ACS APPLIED MATERIALS & INTERFACES

www.acsami.org

Research Article

Innovative Integration of Phase-Change Microcapsules with Metal–Organic Frameworks into an Intelligent Biosensing System for Enhancing Dopamine Detection

Jingjing Li, Jinghua Yu, Zhao Sun, Huan Liu,* and Xiaodong Wang*

Cite This: *ACS Appl. Mater. Interfaces* 2021, 13, 41753–41772

Read Online

ACCESS | Metrics & More | Article Recommendations | Supporting Information

ABSTRACT: This work focuses on an interdisciplinary issue in energy management and biosensing techniques. Aiming at enhancing the biosensing detection of dopamine at high ambient temperatures, we developed an innovative integration of phase-change microcapsules with a metal–organic framework (MOF) based on zeolitic imidazolate framework-8 to develop an intelligent electrochemical biosensing system with a thermal self-regulation function. We first fabricated a type of electroactive microcapsules containing a MOF-anchored polypyrrole/SiO_2 double-layered shell and a phase-change material (PCM) core. The resultant microcapsules not only exhibit a regular spherical morphology with a layer-by-layer core–shell microstructure but also display an effective temperature-regulation capability to enhance enzymatic bioactivity under phase-change enthalpies of around 124.0 $J{\cdot}g^{-1}$ along with good thermal impact resistance and excellent thermal cycling stability for long-term use in thermal energy management. These electroactive microcapsules were then used to modify a working electrode together with laccase as a biocatalyst to construct a thermal self-regulatory biosensor. With a high sensitivity of 3.541 $\mu A{\cdot}L{\cdot}\mu mol^{-1}{\cdot}cm^{-2}$ and a low detection limit of 0.0069 $\mu mol{\cdot}L^{-1}$ at 50 °C, this biosensor exhibits much better determination effectiveness toward dopamine at higher temperatures than conventional biosensors thanks to *in situ* thermal management derived from its PCM core in the electroactive microcapsules. This study offers a promising approach for development of intelligent thermal self-regulatory biosensors with an enhanced detection capability to identify various chemicals accurately in a wide range of applicable temperatures.

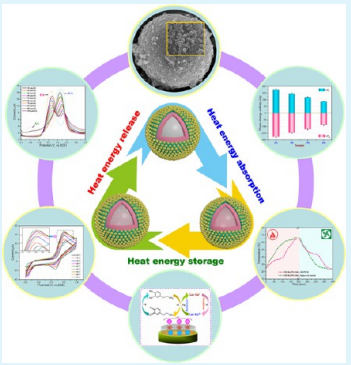

KEYWORDS: *intelligent biosensor, thermal self-regulation, electroactive phase-change microcapsules, dopamine, biosensing detection*

INTRODUCTION

Phase-change materials (PCMs) are well known as a group of latent-heat-storage materials that are capable of storing huge amounts of thermal energy through a transformation in the physical state at an almost constant temperature. Having the advantages of a simple and reliable structure, small size, broad phase-change temperature selection range, and obvious energy-saving effects, PCMs are of particular interest as they can provide a remarkable increase in heat capacity along with very small or negligible temperature change in comparison with traditional sensible heat energy-storage materials.[1] Therefore, PCMs exhibit broad application prospects for energy management systems to implement heat energy storage and temperature regulation in a high-efficient and economical way.[2,3] Nevertheless, most of commonly used PCMs like various fatty acids, paraffin waxes, inorganic molten salts, salt hydrates, and their eutectics are doomed to undergo repetitive solid–liquid state transitions in the heat charging–discharging process.[4] In many of the PCM applications, the high fluidity of PCMs in the molten state is cited as a critical shortcoming. This not only results in a fundamental difficulty with the handling of PCMs but also makes them suffer from leakage, osmosis, and flowing away during the operating process. The other disadvantages of PCMs include a considerable change in volume during phase transition, low thermal conductance, high supercooling, corrosiveness, evaporation, and decomposition, and each of them deteriorates the phase-change performance and heat-storage capability of PCMs.[5] Therefore, solid–liquid PCMs are not considered to be a good candidate for use in their bulk state.[6] Microencapsulation of PCMs is recognized as an effective solution to address their inherent drawbacks and has already been proven as a successful technology in commercial applications. By means of microencapsulation technology, PCMs are engulfed in a compatible thin solid shell to form small capsules with varying diameters from 1 μm to 1 mm.[7] A variety of shell materials, including inorganic materials, organic polymers, and their composites or hybrids, have been used for microencapsulating PCMs. The formation of the capsule shell

Received: July 16, 2021
Accepted: August 19, 2021
Published: August 30, 2021

https://doi.org/10.1021/acsami.1c13446
ACS Appl. Mater. Interfaces 2021, 13, 41753–41772

offers good protection and tight sealing for PCMs to overcome leakage and osmosis problems and also avoids possible contact and interactions for PCMs with the surrounding environment.[8,9] The utilization of heat charging and discharging features of PCMs and their microencapsulation products in the phase-change process for multifunctional and multipurpose applications has been an active research trend in recent years.[10] This can be realized by integrating a PCM core with a functionalized shell. Such a smart integration can combine the unique heat-storage capability of the PCM core with the special functions from the functional shells attributed to their intrinsic performance, such as photocatalytic, fluorescent, antibacterial, superparamagnetic, gas-sensitive, and thermochromic properties.[11−13] With the rapid development of microencapsulation technology, the bi- or multifunctional phase-change microcapsules can be feasibly obtained through encapsulating PCMs either in a composite/hybrid material or with a hierarchical structural shell. As a result of this development, an increasing number of innovative phase-change microcapsules have been created with the promise of original properties and multipurpose applications.[14]

Functional phase-change microcapsules can be custom-designed to meet specific requirements for biological and electrochemical applications. Such a research direction has been receiving great attention in recent years. It is well known that enzymes as a family of essential biocatalysts have a high thermal sensitivity and show a high biocatalytic activity only in an optimum temperature range.[15] Similarly, electroactive materials also exhibit an optimal electrochemical behavior without accelerated aging and recycling capacity fade in a suitable working temperature region because there is a variety of exothermic redox reactions taking place in the reversible oxidation−reduction process.[16] Therefore, it is definitely necessary to establish a thermal management system for the above-mentioned two applications to perform temperature regulation and control *in situ* to enhance their biocatalytic and electrochemical effectiveness in a broad temperature range.[17,18] As a result of this target, an innovative integration of biocatalytic or electrochemical functions and thermal management effectiveness has been successfully realized by fabricating various bifunctional phase-change microcapsules. In the resultant bifunctional phase-change microcapsules, the custom-designed functional shell can offer the designated function, while the PCM core serves as a thermal management source for temperature regulation to buffer thermal swings *in situ*. Many methods have been developed using various approaches to fabricate the bifunctional phase-change microcapsules for biological and electrochemical applications. Li et al.[19] and Jiang et al.[20] developed two types of innovative thermal self-regulatory enzyme carriers based on the PCM-containing bifunctional microcapsules to immobilize amylases and lipase for enhancing its biocatalytic activity in high ambient temperatures. Cao et al.[21] developed a thermal self-regulatory enzyme carrier with enhanced enzymatic activity through microencapsulating PCM with a SiO_2/polydopamine/gold nanoparticles layer-by-layer shell, followed by immobilizing laccase using a copper chelate method. Moreover, Xu et al.[22] fabricated the phase-change microcapsules based on a SiO_2/MnO_2 hierarchical shell with enhanced electrochemical performance resulting from the thermal regulation of their PCM core at a high operating temperature. Sun et al.[23] designed a smart electrode material with a thermal self-regulatory function through microencapsulating PCMs in a polyaniline/carbon nanotube-functionalized shell for electrochemical enhancement in a high-temperature environment. These findings provided new approaches for development of bi- and multifunctional phase-change microcapsules for biological and electrochemical applications.

Dopamine (DA) is one of the most effective neurotransmitters in mammalian central nervous systems, and it can serve as a chemical messenger between the brain and neurons, playing a critical role in the neurochemical and neurohormonal functions in the human and mammalian brains.[24] The rapid, accurate, and sensitive detection of DA plays a critical role in clinical diagnosis for neurological illnesses.[25] The electrochemical biosensing detection has been regarded as one of the most effective methods in the determination of DA because it can provide practicality, sensitivity, and fast response. In an electrochemical biosensor, enzymes are usually used as biological recognition molecules to generate a chemical signal when reacting with the detected substrates, while electrodes are employed to translate the chemical signal into an electrical signal.[26] In this sense, both biocatalysis and redox reactions are involved in the electrochemical biosensing detection. In the clinical application of DA biosensors, the ambient temperature for DA detection may be variable. The use of current DA detection devices is limited by the fragile nature of enzymes such as tyrosinase and polyphenol oxidase due to their narrow temperature ranges and higher requirements for the pH environment.[27] Therefore, high ambient temperatures are evidently disadvantageous to the detection and determination of DA when using an electrochemical biosensing method. In this sense, there is an emerging requirement for developing high-efficient and facile thermal management techniques for fabricating DA detection devices that can be used under harsh conditions. The techniques currently used, including semiconductive temperature control, coolants, and polymerase chain reaction, have been applied for the temperature control of electrochemical sensors.[28,29] However, the realization of these techniques needs additional devices to implement heating and cooling to maintain a constant ambient temperature, increasing the size of DA detection devices along with an extra cost. This may bring about inconvenience in operating and poor cost-effectiveness for DA assay.

To address this shortcoming of biosensors for the determination of DA, we focused on an innovative integration of phase-change microcapsules with metal−organic frameworks for enhancing the electrochemical biosensing detection to DA under *in situ* thermal management in this work. We constructed a type of novel phase-change microcapsules based on a paraffin-type PCM core, a SiO_2 inner shell, and an electroactive layer based on the zeolitic imidazolate framework-8 (ZIF-8)/polypyrrole (PPy) composite. As a type of important metal−organic frameworks (MOFs), ZIF-8 is recognized as a good modifier for an electrochemical sensor when bound with conducting polymers such as PPy.[30,31] Therefore, the resultant microcapsules were expected to achieve a high electrochemical activity and good biocompatibility from their functional outer layer together with the thermal management effectiveness of their PCM core. Such a type of bifunctional phase-change microcapsules was used to modify the working electrode to construct an intelligent biosensor with a thermal self-regulation function. By means of this intelligent biosensor, DA can be detected and determined more accurately, sensitively, and rapidly through buffering

https://doi.org/10.1021/acsami.1c13446
ACS Appl. Mater. Interfaces 2021, 13, 41753−41772

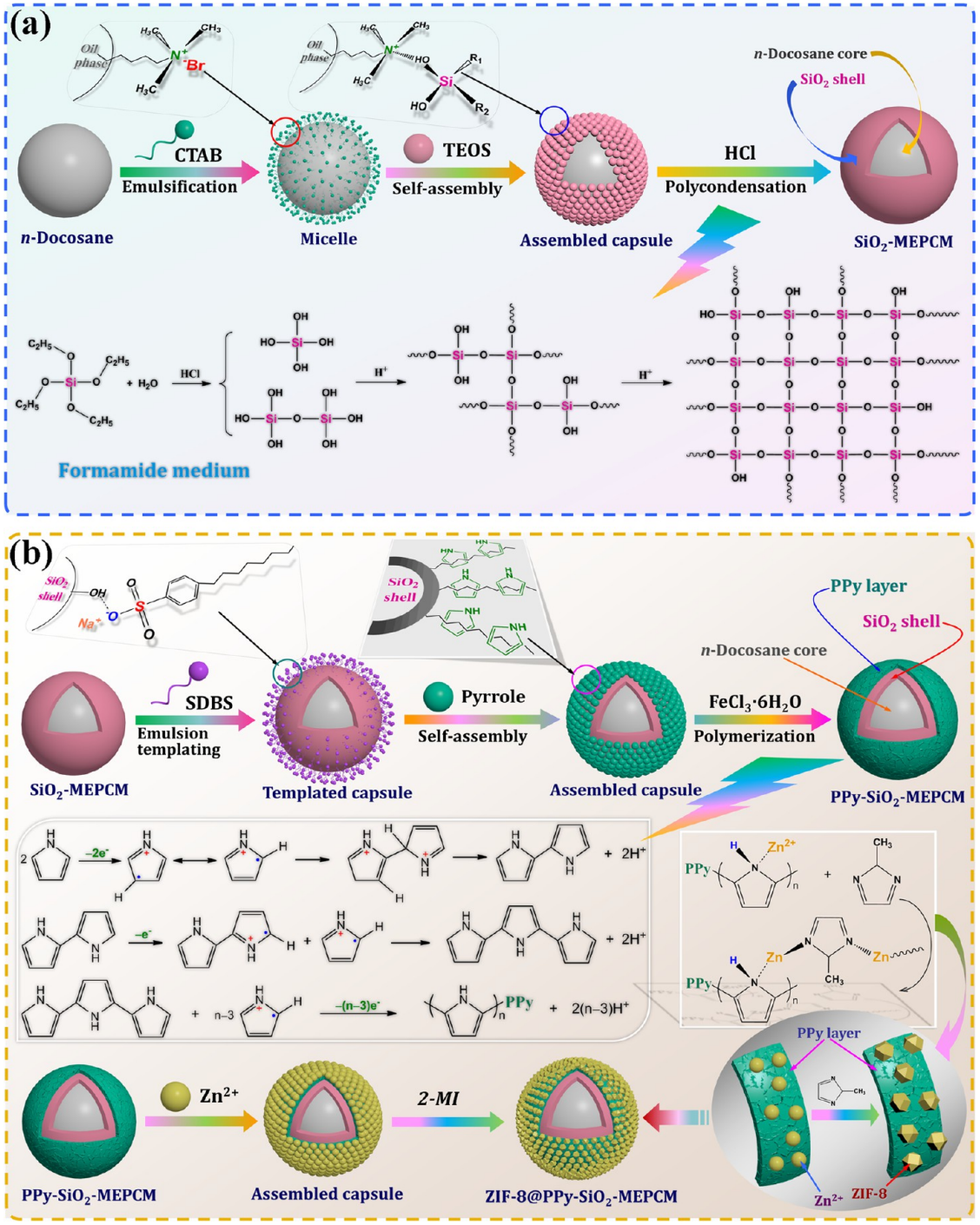

Figure 1. Schemes of fabrication strategies and reaction mechanisms for (a) the SiO_2-MEPCM and (b) ZIF-8@PPy-SiO_2-MEPCM.

thermal swings in the biosensing system at higher operating temperatures or under the drastic fluctuation of ambient temperature. The design strategy, fabrication methodology, microstructures, thermal performance, and thermal management behaviors of the phase-change microcapsules were analyzed in detail in this paper. The electrochemical behaviors and determination capability of the resultant biosensor for DA were particularly discussed under different operating temperatures. It is anticipated that the intelligent biosensor designed in this study can perform temperature regulation and thermal management *in situ* through its PCM core without extra device and cost. With a rapid thermal response from the phase-change microcapsules in the electrode, a real-time temperature control can be conducted *in situ* for this biosensor, which can control the microenvironmental temperature around the electrode. This method is more effective, economical, and convenient for DA detection. This study offers a new approach for development of intelligent thermal self-regulatory biosensors to meet the requirement for the accurate and high-efficient detection of biochemicals over a wide temperature range.

MATERIALS AND METHODS

Materials. *N*-Docosane (99.0 wt %), tetraethoxysilane (TEOS, 98.0 wt %), dopamine hydrochloride (DAH, 98.0 wt %), pyrrole,

https://doi.org/10.1021/acsami.1c13446
ACS Appl. Mater. Interfaces 2021, 13, 41753−41772

potassium ferrocyanide trihydrate [$K_4Fe(CN)_6{\cdot}3H_2O$], uric acid (UA), ascorbic acid (AA), and laccase (≥20 U·mg^{-1}) were commercially supplied by Shanghai Macklin Biochemical Co., Ltd., China. Sodium dodecyl benzene sulfonate (SDBS, 98.0 wt %), cetyltrimethyl ammonium bromide (CTAB, 98.0 wt %), formamide, *N*,*N*-dimethylformamide (DMF), zinc nitrate hexahydrate [$Zn(NO_3)_2{\cdot}6H_2O$], ferric chloride hexahydrate ($FeCl_3{\cdot}6H_2O$), potassium chloride (KCl), 2-methylimidazole (2-MI, ≥98.0 wt %), HCl aqueous solution (37.5 wt %), and absolute ethanol were purchased from Tianjin Fuchen Chemical Reagent Co. Ltd., China. A Nafion perfluorosulfonic acid (PFSA) polymer dispersion (5.0 wt %) was provided by Shanghai Aladdin Biochemical Technology Co., Ltd., China. All of the reagents were of analytical grade and used as received.

Synthesis of Base Phase-Change Microcapsules. At the start of the experiment, the core−shell structural *n*-docosane/silica phase-change microcapsules (named as SiO_2-MEPCM) were synthesized with TEOS as a silica source and *n*-docosane as a core material through emulsion-templated interfacial polycondensation based on the synthetic route schematically illustrated in Figure 1a. In a typical procedure, a 500 mL three-necked round-bottom flask was charged with *n*-docosane (8.0 g) and TEOS (8.0 g), and the resultant mixture was stirred at 50 °C for 1 h. Formamide (150.0 mL) as a dispersion medium and CTAB (3.0 g) as a cationic surfactant were mixed in another beaker under agitation for 1 h and then poured into the flask. The resulting mixture was allowed to emulsify under vigorous agitation for 1.5−2.0 h to obtain a homogenous emulsion. An HCl aqueous solution (pH −0.25, 180.0 mL) was then added dropwise into the flask to induce the hydrolysis and interfacial polycondensation of TEOS. The reactant mixture was allowed to react for 3−4 h under agitation. The reactant was subsequently aged in a water bath at 50 °C for 24 h, and then it was filtered, washed, and dried in an oven at 35 °C for 48 h to achieve the SiO_2-MEPCM.

Fabrication of ZIF-8/PPy-Coated Phase-Change Microcapsules. To fabricate a ZIF-8/PPy composite layer onto the SiO_2-MEPCM, a PPy coating layer was first deposited on the shell surface through an oxidation polymerization reaction to form the PPy-coated SiO_2-MEPCM (named as PPy-SiO_2-MEPCM). Figure 1b shows the schematic fabrication route and reaction mechanisms for the PPy-SiO_2-MEPCM. In a typical procedure, deionized water (150.0 mL), SiO_2-MEPCM (10.0 g), and SDBS (5.0 g) as an anionic surfactant were mixed in a 500 mL three-necked round-bottom flask under agitation at room temperature. An aqueous HCl solution (1.0 mol·L^{-1}) was poured into the flask with agitation for 20 min to obtain a suspension at pH 3−4. The flask was moved to an ice bath, and then pyrrole (2.0 ml) was poured into the flask under mechanical agitation at 0 °C for 1 h. An $FeCl_3$ aqueous solution (0.5 mol·L^{-1}, 50.0 mL) was added to induce an oxidation polymerization reaction. The reactant suspension was allowed to react under agitation at 0 °C for 4−5 h, and the resultant product was filtered, washed, and dried in an oven at 35 °C for 24 h to obtain the PPy-SiO_2-MEPCM.

Following the formation of the PPy-SiO_2-MEPCM, ZIF-8 nanocrystals were anchored onto the surface of the PPy-SiO_2-MEPCM through a self-assembly growth to form the PPy-SiO_2-MEPCM with surface-anchored ZIF-8 (named as ZIF-8@PPy-SiO_2-MEPCM). In a typical procedure, a 500 mL three-necked round-bottom flask was charged with PPy-SiO_2-MEPCM (10.0 g), $Zn(NO_3)_2{\cdot}6H_2O$ (10.0 g), and ethanol (100.0 mL), and the resultant mixture was stirred at 30 °C for 2 h. 2-MI (12.0 g) was dissolved in 100 mL of ethanol in another beaker, and the resultant solution was poured into the flask to induce a coordination reaction. The reactant mixture was allowed to react at 30 °C for 1 h under agitation. The resultant product was filtered, washed with DMF, and dried in an oven at 35 °C for 24 h to obtain the ZIF-8@PPy-SiO_2-MEPCM. To facilitate a comparative investigation, the ZIF-8@PPy-coated silica microspheres were also fabricated as a control without a PCM core under identical conditions and named as ZIF-8@PPy-SiO_2-SPR.

Preparation of the Working Electrode Based on ZIF-8@PPy-SiO_2-MEPCM. A glassy carbon electrode (GCE) was surface finished and then rinsed with ethanol and deionized water, followed by drying with a nitrogen stream. The clean GCE was modified with the ZIF-8/PPy@SiO_2-MEPCM. In a typical procedure, the ZIF-8/PPy@SiO_2-MEPCM (0.5 mg) was dispersed in a Nafion PFSA polymer dispersion (1.0 wt %, 50.0 μL) with the aid of ultrasonication for 1 h to form a homogenous suspension. The suspension (6.0−7.0 μL) was dripped on the surface of the clean GCE, followed by drying at room temperature for 2−3 h to obtain the ZIF-8/PPy@SiO_2-MEPCM-modified GCE. The modified GCE was further decorated with laccase by dripping a laccase-containing phosphate buffer solution (PBS, 0.1 mol·L^{-1}, pH 7.2−7.4) on its surface and then allowed to dry at 4 °C for 4 h to obtain a working electrode required for the construction of electrochemical biosensors.

Characterization and Measurements. Scanning electron microscopy (SEM) was performed using a Zeiss SUPRA 55 field-emission scanning electron microscope at an acceleration voltage of 20 kV. Image analysis was performed for the resultant SEM images to determine the mean grain size and distribution of microcapsules by means of NanoMeasure software. Transmission electron microscopy (TEM) was performed using a JEOL JEM 2100 transmission electron microscope at an acceleration voltage of 100 kV. Surface elemental analysis was carried out using an Oxford INCAX-Act energy-dispersive X-ray (EDX) spectrometer. The surface chemical compositions and atomic states of microcapsule samples were characterized using a Thermo Fisher Scientific EscaLab 250Xi X-ray photoelectron spectrometer (XPS) equipped with a monochromatized Al Kα radiation source (1486.6 eV) and a hemispherical analyzer with a pass energy of 20 eV. An energy step size of 0.1 eV was used to analyze the elemental composition and elemental electron binding energy of microcapsule samples. The resultant core-level XPS spectra were fitted with Casa XPS software, and their deconvolution was further optimized through a Lorentzian-Gaussian peak-shape method. X-ray powder diffraction (XRD) was performed using a Japan Rigaku D/Max 2500 VB2 + P/C X-ray diffractometer with Cu Kα radiation (λ = 0.1541 nm). Fourier-transform infrared (FTIR) spectroscopy was performed on a Thermo Scientific Nicolet iS10 infrared spectrometer using a sampling method by KBr compression. Infrared spectra were recorded in the wavelength range of 400−4000 cm^{-1} at a resolution of 2 cm^{-1}. N_2 adsorption/desorption isotherms were recorded at 77 K using a Micromeritics ASAP 2020 sorptometer. Pore size distribution and specific surface area were determined by means of the Barrett−Joyner−Halenda (BJH) and Brunauer−Emmett−Teller (BET) models, respectively.

Differential scanning calorimetry (DSC) measurements were carried out using a TA Instruments Q20 differential scanning calorimeter at a ramp rate of 10 °C·min^{-1} under a nitrogen flux of 50 mL·min^{-1}, crystallization peak temperature (T_c), crystallization enthalpy (ΔH_c), melting peak temperature (T_m), and melting enthalpy (ΔH_m) were obtained from DSC analysis. Indium was used as a standard to calibrate the changes of phase-change temperature and enthalpy. Thermogravimetric analysis (TGA) was carried out under a nitrogen atmosphere using a TA Instruments Q50 thermogravimetric analyzer with a ramp rate of 10 °C·min^{-1}. Thermal conductivity was measured with an HS-DR-5 thermal conductivity tester (Shanghai HESHENG Instruments, China) through a transient plane source method. This instrument has an accuracy of ±3% and a measurement range of 0.005−300 W·m^{-1}·K^{-1}. The measurement was carried out directly using the powders of a microcapsule sample at room temperature, and each test was performed at least five times until the mean deviation was less than 3%. An analytical balance method was adopted to evaluate the antileakage performance of microcapsule samples. A certain quantity of the microcapsule sample was kept in an oven at 90 °C. The sample was taken out and weighed at an interval of 1.5 h, and its leakage rate (L_R, wt %) was determined using the following equation[32]

$$L_R = \frac{m_0 - m_t}{m_0} \times 100\% \quad (1)$$

where m_0 (g) and m_t (g) represent the masses obtained at the initial time and arbitrary time during the heating process, respectively. A Testo 875-1i versatile thermal imager was employed to characterize

https://doi.org/10.1021/acsami.1c13446
ACS Appl. Mater. Interfaces 2021, 13, 41753−41772

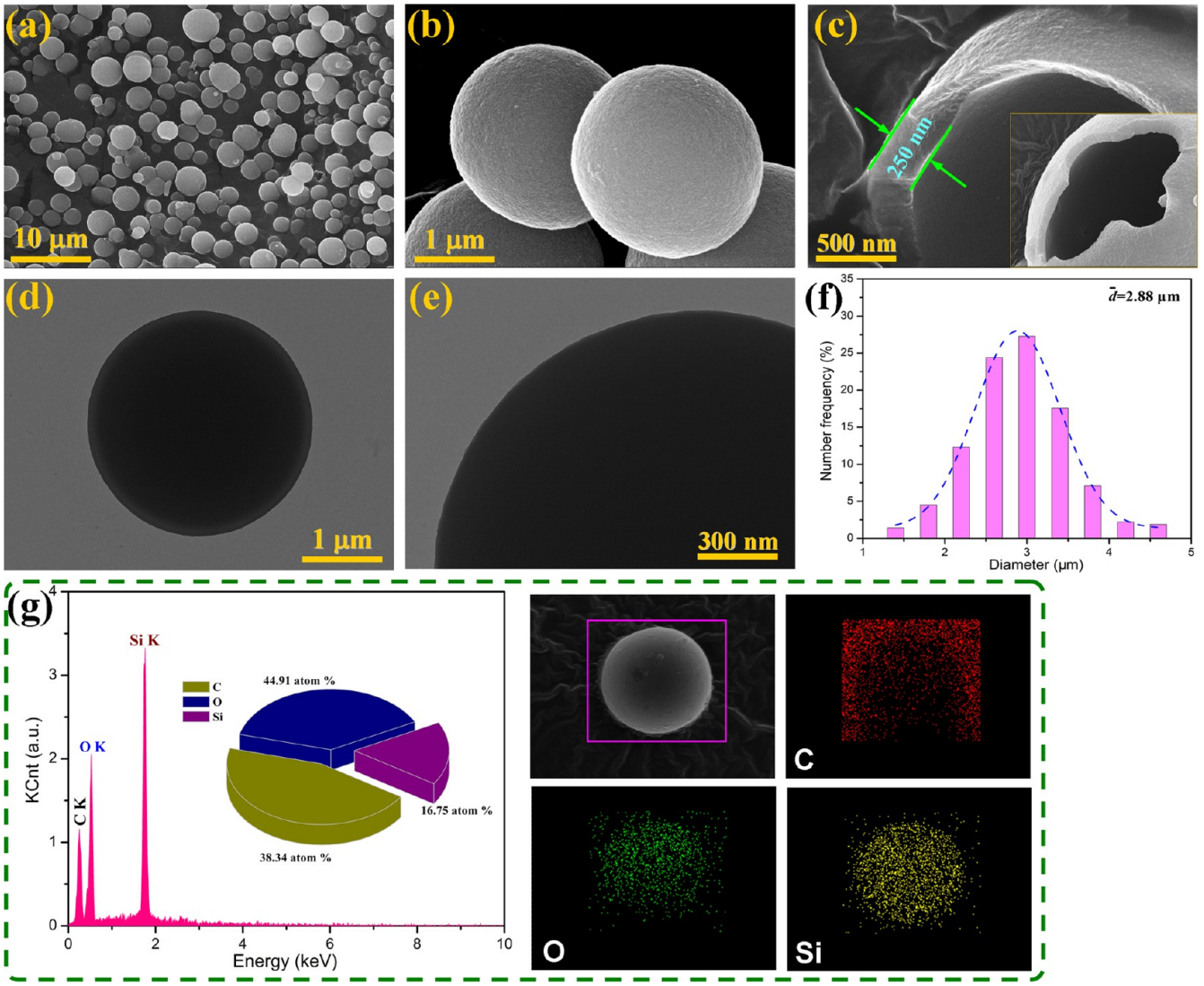

Figure 2. (a–c) SEM micrographs, (d, e) TEM images, (f) the grain-size distribution curve, and (g) the EDX spectrum and elemental mapping images of the SiO_2-MEPCM.

the temperature regulation and thermal management behaviors of microcapsule samples. Infrared thermographic images were recorded at an accuracy of ±1 °C and image resolution of 640 × 480. Testo ComSoft Basic software was used to read out the surface temperatures recorded by data loggers. A heat-impact experiment was conducted to examine the form and shape stabilities of microcapsules. All samples were subjected to isothermal heating at 120 °C on an IKA C-MAG HP10 high-precision electronic hot plat, and their aspects were monitored in real-time by a digital camera.

A custom-designed three-electrode electrochemical cell was established to carry out electrochemical analysis using a Chenhua CHI760E electrochemical workstation with a potential accuracy of ±1.0 mV. The electrochemical cell was configured with a working electrode, a Pt counter electrode, and a saturated calomel electrode (SCE) as a reference electrode. An aqueous solution containing $K_4Fe(CN)_6$ (2.0 mmol·L^{-1}) and KCl (0.1 mol·L^{-1}) was used as an electrolyte for the cell. Two different types of working electrodes were fabricated by modifying a GCE, respectively, with the ZIF-8/PPy@SiO_2-MEPCM and ZIF-8/PPy@SiO_2-SPR, followed by decorating with laccase. These two different working electrodes were evaluated by differential pulse voltammetry (DPV), cyclic voltammetry (CV), and electrochemical impedance spectroscopy (EIS) in the temperature range of 25–65 °C with an interval of 5 °C. CV curves were obtained in the scan range between −0.4 and 0.4 V, and the scan rate was set to be 100 mV·s^{-1}. DPV curves were obtained in a scan range from −0.2 to 0.8 V with a step potential of 4 mV. Nyquist plots were obtained from EIS analysis in a frequency ranging from 0.01 to 100 000 Hz.

RESULTS AND DISCUSSION

Fabrication Mechanism and Structural Characterization. To fabricate a ZIF-8/PPy double outer layer onto phase-change microcapsules, the SiO_2-MEPCM was first synthesized using an emulsion-templated interfacial polycondensation technology. Figure 1a shows its schematic synthetic route and reaction mechanisms. In the current work, *n*-docosane was used as a PCM core thanks to its high latent-heat capacity, and it was encapsulated in a compact inorganic SiO_2 shell. The weight ratio of the *n*-docosane core and the silica source (TEOS) was determined to be 50/50 for the synthesis of the microcapsules to obtain a rational balance between the latent-heat capacity and shell thickness based on our previous studies.[21,23] Figure 2 shows the morphology and surface elemental distribution of the SiO_2-MEPCM. It can be seen in Figure 2a–c that the SiO_2-MEPCM presents a regular spherical morphology with a compact and smooth surface. A

https://doi.org/10.1021/acsami.1c13446
ACS Appl. Mater. Interfaces 2021, 13, 41753–41772

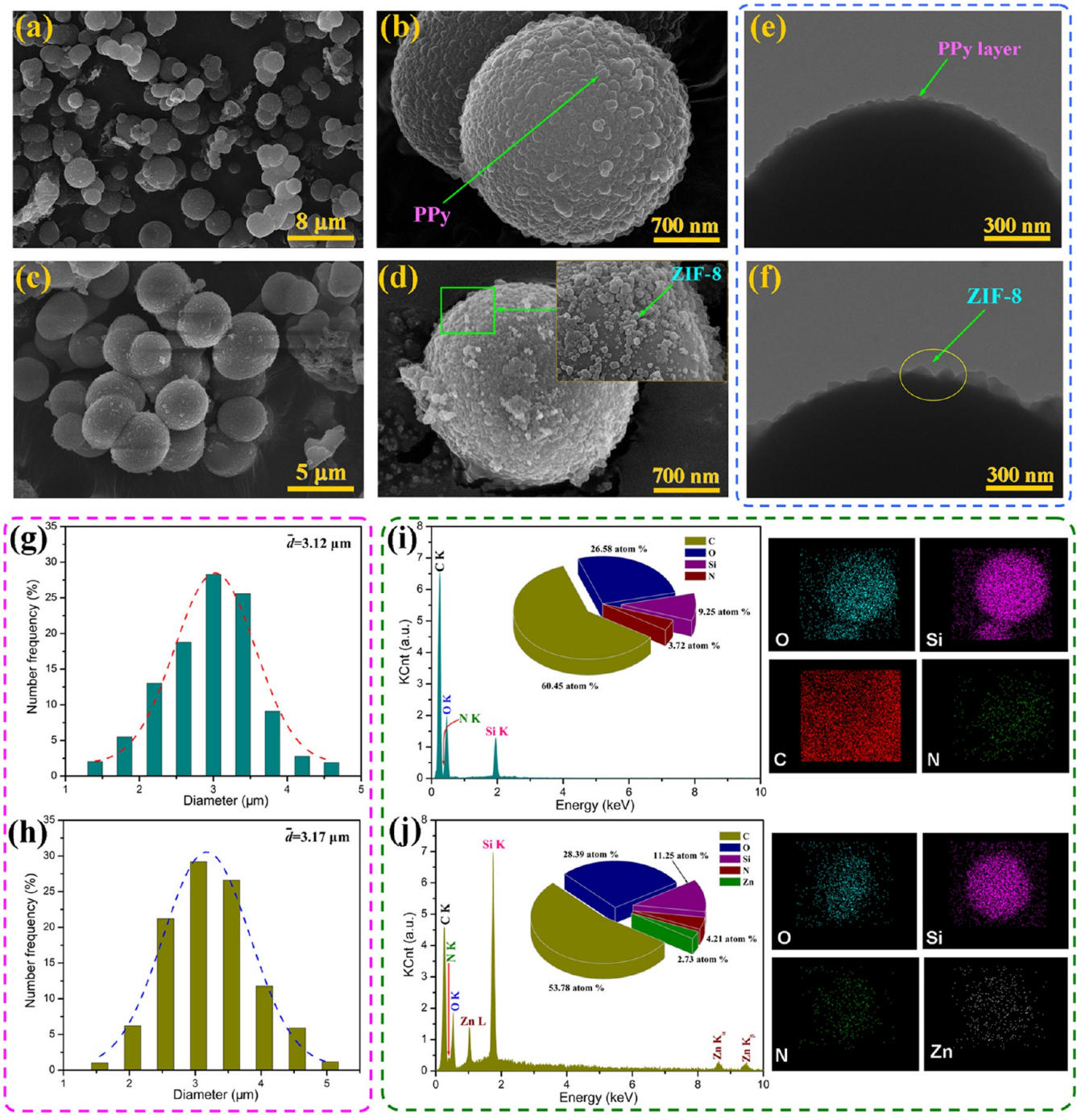

Figure 3. SEM images of (a, b) the PPy-SiO_2-MEPCM and (c, d) ZIF-8@PPy-SiO_2-MEPCM. TEM images of (e) the PPy-SiO_2-MEPCM and (f) ZIF-8@PPy-SiO_2-MEPCM. Grain-size distribution curves of (g) the PPy-SiO_2-MEPCM and (h) ZIF-8@PPy-SiO_2-MEPCM. EDX spectra and corresponding mapping images of (i) the PPy-SiO_2-MEPCM and (j) ZIF-8@PPy-SiO_2-MEPCM.

well-fined core−shell microstructure of the SiO_2-MEPCM was identified from the SEM image of broken microcapsules as presented in Figure 2c. Meanwhile, its shell thickness was determined to be around 250 nm. It should be mentioned that these broken microcapsules were obtained through manual grinding. Furthermore, the core−shell microstructure of the SiO_2-MEPCM was also proved by the TEM images as shown in Figure 2d,e. As seen in Figure 2f, the average diameter of the SiO_2-MEPCM can be determined to be 2.88 μm with a narrow grain-size distribution from 1.4 to 4.6 μm. Figure 2g shows the EDX spectrum of the SiO_2-MEPCM as well as the corresponding elemental mapping images. It can be seen that there are a series of intensive peaks related to the C, O, and Si elements in the EDX spectrum, and meanwhile, the mapping images show homogeneous elemental distributions of O and Si on the microcapsule surface along with a distribution of carbon background in the testing environment. These results provide evidence for the successful formation of the SiO_2-MEPCM.

Following the formation of the SiO_2-MEPCM, its surface was deposited with a PPy conductive layer to construct the PPy-SiO_2-MEPCM through oxidation polymerization. According to the synthetic strategy depicted in Figure 1b, SDBS as an

https://doi.org/10.1021/acsami.1c13446
ACS Appl. Mater. Interfaces 2021, 13, 41753−41772

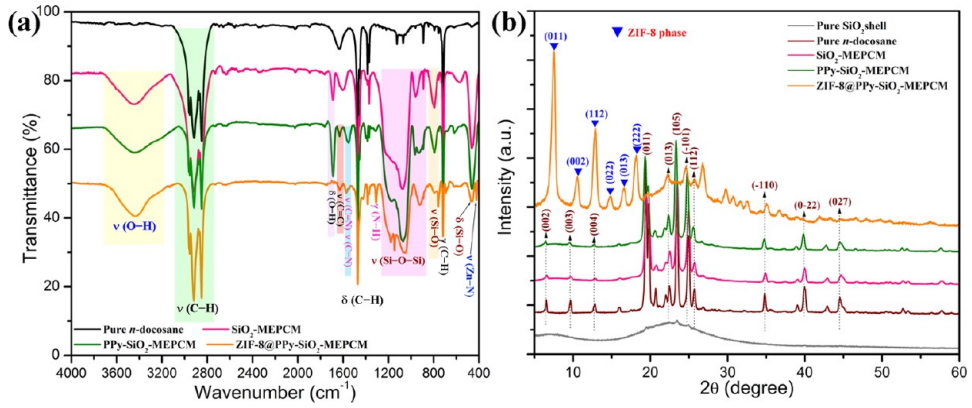

Figure 4. (a) FTIR spectra and (b) XRD patterns of pure *n*-docosane, the SiO_2 shell, and microcapsule samples.

anionic surfactant was first adsorbed onto the surface of the SiO_2-MEPCM *via* intermolecular hydrogen bonding. Then, the alkyl molecular segment of SDBS induced organic pyrrole monomers to assemble on the shell surface. These pyrrole monomers were oxidized by $FeCl_3$ to form radical cations. A number of bipyrrole molecules were generated between the adjacent radical cations by radical coupling and deprotonation, and these bipyrroles were further connected to each other. Such a propagation process was repeated consecutively through reoxidization and coupling, finally leading to the formation of the PPy-SiO_2-MEPCM with a PPy coating layer on the surface of the SiO_2-MEPCM. In succession, ZIF-8 nanocrystals were anchored on the surface of the PPy coating layer through a coordination reaction. The PPy-SiO_2-MEPCM was first dispersed in Zn^{2+} solution, allowing free Zn^{2+} ions to be adsorbed on the surface of a negatively charged PPy coating layer with the aid of electrostatic attraction.[33] The coordination reaction between the Zn^{2+} ions and PPy was then induced by 2-MI, leading to the heterogeneous nucleation of ZIF-8 to form seed nanocrystals upon the surface of the PPy coating layer. These seed nanocrystals can act as crystal nuclei to promote the growth of large-sized ZIF-8 polyhedra. The ZIF-8@PPy-SiO_2-MEPCM was finally obtained from a successive crystal growth. Figure 3a–f shows the SEM and TEM images of the resultant PPy-SiO_2-MEPCM and ZIF-8@PPy-SiO_2-MEPCM. A very rough surface was observed from the PPy-SiO_2-MEPCM due to the formation of a PPy coating layer, as seen in Figure 3a,b. The surface of the ZIF-8@PPy-SiO_2-MEPCM was found to become much rougher with the presence of ZIF-8 nanocrystals (see Figure 3c,d). There is no damage or defect observed from the PPy-SiO_2-MEPCM and ZIF-8@PPy-SiO_2-MEPCM, indicating that these two microcapsule samples have good mechanical strength and structural stability in their layer-by-layer shells. Moreover, the TEM images in Figure 3e,f also demonstrate the existence of the PPy coating layer and the ZIF-8-anchored PPy coating layer in the PPy-SiO_2-MEPCM and ZIF-8@PPy-SiO_2-MEPCM, respectively. According to the SEM image analysis presented in Figure 3g,h, the mean diameters of the PPy-SiO_2-MEPCM and ZIF-8@PPy-SiO_2-MEPCM were determined to be 3.12 and 3.17 μm, respectively. Compared to the SiO_2-MEPCM, there is an increase in shell thickness by 0.24 μm for the PPy-SiO_2-MEPCM and 0.29 μm for the ZIF-8@PPy-SiO_2-MEPCM. These results prove the successful fabrication of the ZIF-8@PPy-SiO_2-MEPCM with the desired morphology and microstructure in accordance with our design strategy.

The surface elemental compositions and distributions of the PPy-SiO_2-MEPCM and ZIF-8@PPy-SiO_2-MEPCM were investigated by EDX spectroscopy, with the resultant spectra and elemental mapping images presented in Figure 3i,j. The PPy-SiO_2-MEPCM was found to show four typical signals related to the C, O, N, and Si elements in its EDX spectrum (see Figure 3i). Besides these four elements, the Zn element was also observed from the EDX spectrum of the ZIF-8@PPy-SiO_2-MEPCM (see Figure 3j). The mapping images in Figure 3i show homogeneous distributions of O, Si, and N elements on the PPy-SiO_2-MEPCM because of the formation of the PPy@/SiO_2 layer-by-layer shell. In contrast, the mapping images in Figure 3i clearly display the Zn element distribution together with the Si, O, and N elements on the ZIF-8@PPy-SiO_2-MEPCM, proving the presence of ZIF-8. All microcapsule samples were also characterized by FTIR spectroscopy, and the obtained infrared spectra are given in Figure 4a. A set of characteristic absorption bands related to the SiO_2 shell and *n*-docosane core were observed in the FTIR spectra of the SiO_2-MEPCM, PPy-SiO_2-MEPCM, and ZIF-8@PPy-SiO_2-MEPCM as marked in Figure 4a. This can be considered as an indication of the successful encapsulation of the *n*-docosane core in the SiO_2 shell. Moreover, both the PPy-SiO_2-MEPCM and the ZIF-8@PPy-SiO_2-MEPCM show a set of characteristic absorption peaks at 1633 cm^{-1} (the C=C stretching vibration), 1550 cm^{-1} (the C–N stretching vibration), 1381 cm^{-1} (the N–H stretching vibration), 1307 cm^{-1} (the out-plane ring bending vibration), and 1175 cm^{-1} (the N–H wagging vibration) in their infrared spectra. This suggests the formation of the PPy layer on the SiO_2-MEPCM.[34,35] On the other hand, the ZIF-8@PPy-SiO_2-MEPCM was found to present a series of intensive absorption peaks corresponding to the C = N stretching vibration at 1574 cm^{-1}, the in-plane ring bending vibration at 1150 cm^{-1}, the =C–H wagging vibration at 754 cm^{-1}, and the Zn–N stretching vibration at 418 cm^{-1} in its FTIR spectrum.[36,37] These results give clear evidence for the presence of ZIF-8 on the surface of the PPy-SiO_2-MEPCM.

XRD was conducted to examine the crystallinity and crystalline structure of three microcapsule samples, and the resultant XRD patterns are shown in Figure 4b. As seen in Figure 4b, the XRD pattern of the pure SiO_2 shell only shows a broad diffuse peak, indicating an amorphous nature of the SiO_2 shell. In contrast, pure *n*-docosane exhibits a series of well-defined diffraction peaks in its XRD pattern as marked in Figure 4b, reflecting its excellent crystallinity. It is worth noting that these diffraction peaks of *n*-docosane also appear in the

https://doi.org/10.1021/acsami.1c13446
ACS Appl. Mater. Interfaces 2021, 13, 41753–41772

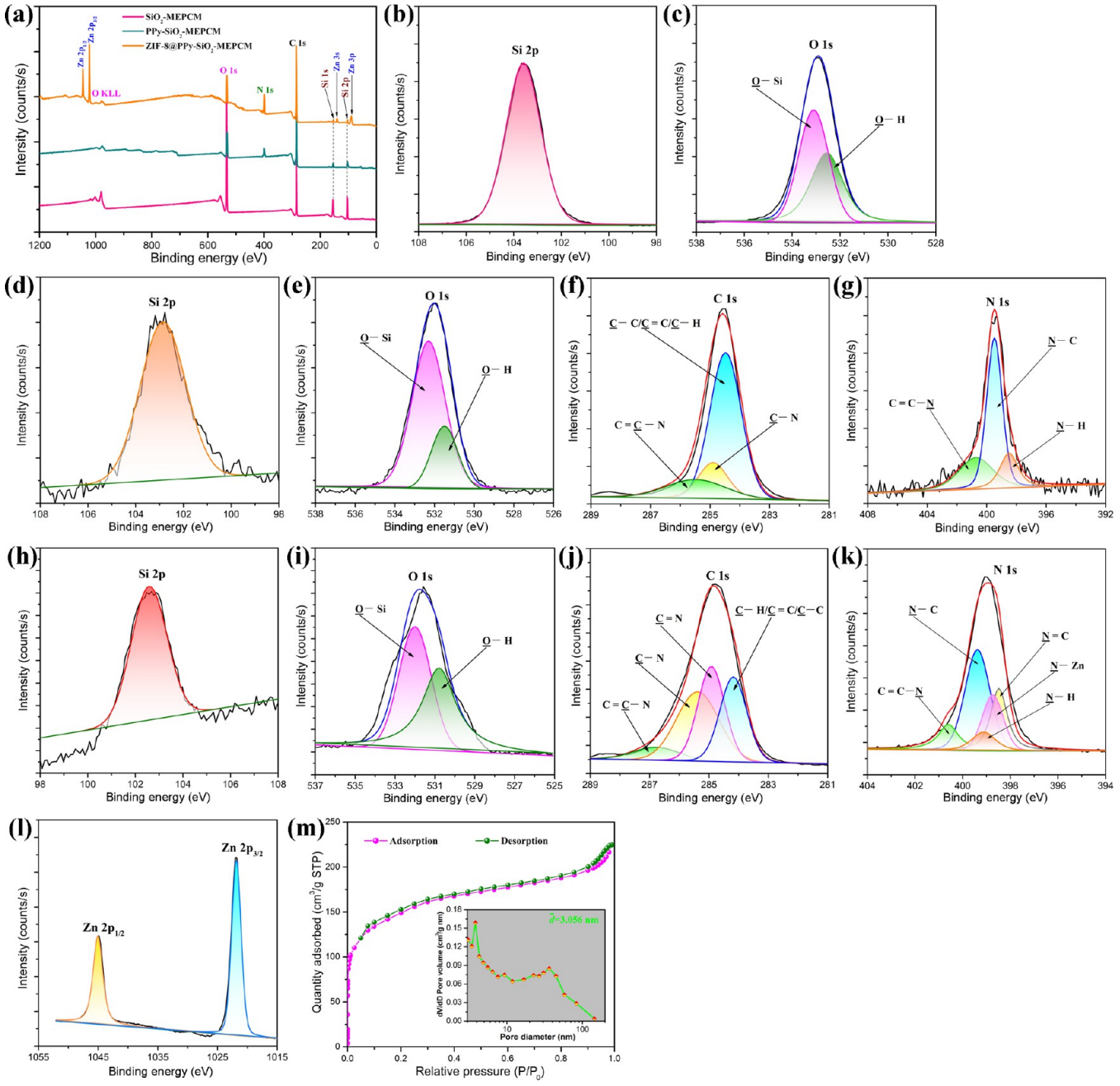

Figure 5. (a) Survey XPS spectra, high-resolution core-level XPS spectra and their deconvoluted curves of (b, c) the SiO_2-MEPCM, (d–g) PPy-SiO_2-MEPCM, (h–l) ZIF-8@PPy-SiO_2-MEPCM. (m) N_2 adsorption–desorption isotherm along with the BJH pore-size distribution curve (inset) of the ZIF-8@PPy-SiO_2-MEPCM.

XRD patterns of the SiO_2-MEPCM, PPy-SiO_2-MEPCM, and ZIF-8@PPy-SiO_2-MEPCM. This means that the layer-by-layer presence of the capsule shell does not influence the crystalline structure of the *n*-docosane core, and its phase-transition capability is maintained well to serve for the thermal management application in biosensors. Moreover, the XRD pattern of the ZIF-8@PPy-SiO_2-MEPCM shows a set of extra diffraction peaks at 7.52, 10.58, 12.89, 14.74, 16.56, and 18.19° corresponding to the assigned reflections of cubic ZIF-8 as marked in Figure 4b. These characteristic diffraction peaks are consistent with the theoretical diffraction patterns as reported in the literature,[36] reconfirming the existence of ZIF-8 crystals on the ZIF-8@PPy-SiO_2-MEPCM.

XPS analysis was conducted for three microcapsule samples to cast light on the chemical structure of their shells in a layer-by-layer mode, and the resultant core-level XPS spectra are shown in Figure 5a–l. As seen in Figure 5a, all of the samples were found to present three characteristic peaks of C, O, and Si atoms in their survey XPS spectra. An extra signal from the N atom appears in the survey XPS spectrum of the PPy-SiO_2-MEPCM, whereas a series of typical Zn signals are observed together with the N signal in the survey XPS spectrum of the ZIF-8@PPy-SiO_2-MEPCM. The atomic coordination state of the Si–O bond can be determined for the SiO_2-MEPCM from its high-resolution core-level XPS spectra of Si 2p and O 1s, as seen in Figure 5b,c. In the case of the PPy@SiO_2-MEPCM, the C═C–N, C═C, C–C, C–H, C═C–N, C–N, N–C, and

https://doi.org/10.1021/acsami.1c13446
ACS Appl. Mater. Interfaces 2021, 13, 41753–41772

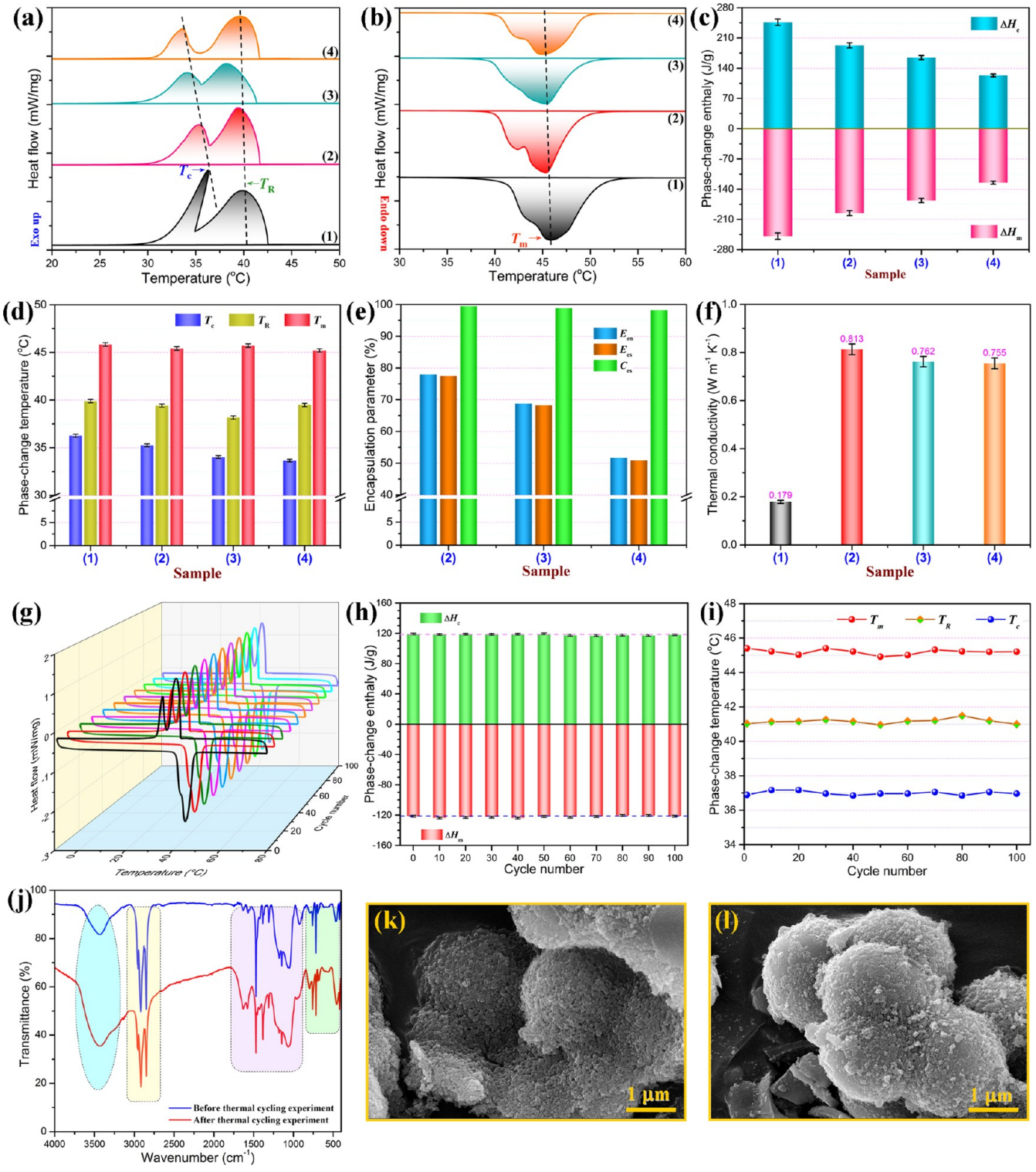

Figure 6. (a) DSC cooling thermograms, (b) DSC heating thermograms, (c) phase-change enthalpies, (d) phase-change temperatures, (e) encapsulation parameters, and (f) thermal conductivities of (1) pure *n*-docosane, (2) SiO_2-MEPCM, (3) PPy-SiO_2-MEPCM, and (4) ZIF-8@PPy-SiO_2-MEPCM. (g) DSC thermograms, (h) phase-change enthalpies, and (i) phase-change temperatures of the ZIF-8@PPy-SiO_2-MEPCM obtained at an interval of thermal cycle number of 10. (j) FTIR spectra of the ZIF-8@PPy-SiO_2-MEPCM obtained before and after the thermal cycling experiment. SEM images of the ZIF-8@PPy-SiO_2-MEPCM obtained (k) before and (l) after the thermal cycling experiment.

N−H bonds, in addition to the Si−O bond, can be identified from its high-resolution XPS spectra as shown in Figure 5d−g. This indicates the coexistence of the SiO_2 shell and the PPy layer in the PPy-SiO_2-MEPCM. In contrast to the PPy-SiO_2-MEPCM, the ZIF-8@PPy-SiO_2-MEPCM displays a set of new signals related to Zn $2p_{1/2}$ (1044.8 eV), Zn $2p_{3/2}$ (1021.9 eV), Zn 3s (139.7 eV), and Zn 3p (88.0 eV) in its high-resolution core-level XPS spectra (see Figure 5a,l). In addition, besides the chemical bonds from the SiO_2 shell and PPy coating layer, the C═N, C═N, and N−Zn bonds can also be found in the

https://doi.org/10.1021/acsami.1c13446
ACS Appl. Mater. Interfaces 2021, 13, 41753−41772

deconvoluted core-level XPS spectra of the ZIF-8@PPy-SiO_2-MEPCM as noted in Figure 5h–k. These results demonstrate the formation of ZIF-8 on the surface of the PPy coating layer. The nanostructural characteristics of the ZIF-8@PPy-SiO_2-MEPCM were characterized through a N_2 adsorption–desorption experiment, with the resultant results presented in Figure 5m. It can be seen that the ZIF-8@PPy-SiO_2-MEPCM displays a typical type I isotherm with an H3 hysteresis loop according to the IUPAC classification. This represents a mesoporous structure appearing on the surface of the ZIF-8@PPy-SiO_2-MEPCM due to the formation of nanostructural ZIF-8. Furthermore, the specific surface area and mean pore size were determined to be 496.1 $m^2 \cdot g^{-1}$ and 3.056 nm by the BET and BJH models, respectively. Such a large specific surface area together with a mesoporous structure not only can promote a fast heat transfer of the ZIF-8@PPy-SiO_2-MEPCM for thermal management but also can lead to an electrochemical response enhancement.

Phase-Change Behaviors and Thermal Performance. The phase-change behaviors and thermal energy-storage properties of microcapsule samples were investigated with dynamic DSC scans, with the resultant DSC thermograms and thermal analysis results presented in Figure 6. It should be noted that there is a bimodal behavior observed from both the crystallization and the melting processes of the microcapsule samples as well as pure *n*-docosane in their DSC thermograms (see Figure 6a,b). Such bimodal exothermic and endothermic behaviors are attributed to the metastable rotator phase appearing in *n*-docosane. It has been reported that *n*-alkanes are normally obliged to experience a rotator phase transformation in the crystallization process as a result of the formation of intrachain defects and conformational disordered crystals.[38,39] The occurrence of bimodal behavior in all of the microcapsule samples suggests that the layer-by-layer formation of the capsule shell seems not to affect the phase-change behaviors of the *n*-docosane core. As observed from the thermal analysis data listed in Figure 6c,d, pure *n*-docosane presents a T_c of 36.3 °C with a ΔH_c of 246.4 $J \cdot g^{-1}$ and a T_m of 45.8 °C with a ΔH_m of 248.7 $J \cdot g^{-1}$. Moreover, pure *n*-docosane also reveals a rotator phase temperature (T_R) at 39.0 °C. These results suggest that *n*-docosane has a high latent-heat capacity and desirable phase-change temperatures for performing temperature regulation in biosensing systems. Nevertheless, all of the microcapsule samples show a decrease in ΔH_c and ΔH_m due to the presence of an inert SiO_2 shell as well as an electroactive PPy/ZIF-8 layer. This evidently reduces the mass fraction of *n*-docosane in the microcapsule system, consequently resulting in a decrease in the melting and crystallization enthalpies of three microcapsule samples in proportion to the mass fraction of shell materials. In this sense, the higher mass fraction of shell materials results in lower phase-change enthalpies for the microcapsule sample. Nevertheless, the ZIF-8@PPy-SiO_2-MEPCM still achieved a high latent-heat capacity of around 124.0 $J \cdot g^{-1}$ after the layer-by-layer encapsulation, indicating a satisfactory heat-storage capacity for thermal management application. Table S1 summarizes the thermal performance of the microcapsule samples synthesized in this work and other microencapsulated paraffin-type PCMs with various SiO_2-based shells reported in the literature (see the Supporting Information). As observed from Table S1, most of the paraffin/SiO_2-based systems presented a bimodal crystallization behavior. However, the SiO_2-MEPCM and PPy-SiO_2-MEPCM synthesized in this work exhibited a higher latent-heat capacity than most of the paraffin/SiO_2-based phase-change microcapsules with a bimodal or unimodal crystallization behavior as reported in the literature. This result indicates that the thermal performance of the paraffin/SiO_2-based phase-change microcapsules is highly related to the encapsulation technique instead of crystallization behaviors. Moreover, it is of importance to note that the ZIF-8@PPy-SiO_2-MEPCM achieved a high latent-heat capacity of over 120 $J \cdot g^{-1}$, which can meet the requirement of thermal management for future use in the intelligent biosensor. In addition, there is a visible reduction in T_c and T_R observed from three microcapsule samples compared to pure *n*-docosane, as seen in Figure 6d. This is ascribed to the geometric confinement of a microsized capsule, which restricts the molecular movement of the *n*-docosane core in the crystallization process. In addition, a slight decrease in T_m is also noted for three microcapsule samples, which may be due to an enhancement in heat transfer in the microcapsule system caused by a large specific surface area of the SiO_2 shell.

Three important encapsulation parameters, including the encapsulation ratio (E_{en}), encapsulation efficiency (E_{es}), and thermal energy-storage efficiency (C_{es}), are usually used for reflecting the encapsulation characteristics of phase-change microcapsules, and they can be determined using the following equations[21]

$$E_{en}\ (\%) = \frac{\Delta H_{m,MEPCM}}{\Delta H_{m,PCM}} \times 100\% \tag{2}$$

$$E_{es}\ (\%) = \frac{\Delta H_{m,MEPCM} + \Delta H_{c,MEPCM}}{\Delta H_{m,PCM} + \Delta H_{c,PCM}} \times 100\% \tag{3}$$

$$C_{es}\ (\%) = \frac{(\Delta H_{m,MEPCM} + \Delta H_{c,MEPCM}) \cdot \Delta H_{m,PCM}}{(\Delta H_{m,PCM} + \Delta H_{c,PCM}) \cdot \Delta H_{m,MEPCM}} \times 100\% \tag{4}$$

where $\Delta H_{m,MEPCM}$ ($J \cdot g^{-1}$) and $\Delta H_{m,PCM}$ ($J \cdot g^{-1}$) are the melting enthalpies of phase-change microcapsules and pure *n*-docosane, respectively, and $\Delta H_{c,MEPCM}$ ($J \cdot g^{-1}$) and $\Delta H_{c,PCM}$ ($J \cdot g^{-1}$) are the crystallization enthalpies of phase-change microcapsules and pure *n*-docosane, respectively. As seen in Figure 6e, the SiO_2-MEPCM exhibits a high encapsulation ratio and encapsulation efficiency of over 77%. In the presence of a PPy coating layer, the PPy@SiO_2-MEPCM shows a decrease in E_{en} and E_{es}, both of which still reached around 70%. The E_{en} and E_{es} of the ZIF-8@PPy-SiO_2-MEPCM are further reduced to approximately 52% due to the incorporation of ZIF-8, indicating that there is about 52% of the *n*-docosane core in the microcapsules ready for thermal energy storage. However, all of the microcapsule samples were found to achieve extreme high C_{es} of over 98%. This suggests that 98% of the *n*-docosane core can normally perform reversible phase transitions to absorb, store, and release thermal energy, reflecting good thermal management effectiveness for future use.

Figure 6f shows the thermal conductivities of pure *n*-docosane and three microcapsule samples. Pure *n*-docosane was found to have a low thermal conductivity of 0.179 $W \cdot m^{-1} \cdot K^{-1}$. Furthermore, the SiO_2-MEPCM, PPy-SiO_2-MEPCM, and ZIF-8@PPy-SiO_2-MEPCM exhibit higher thermal conductivities of 0.813, 0.762, and 0.755 $W \cdot m^{-1} \cdot K^{-1}$, respectively. There is no doubt that the thermal conductance can be significantly

https://doi.org/10.1021/acsami.1c13446
ACS Appl. Mater. Interfaces 2021, 13, 41753–41772

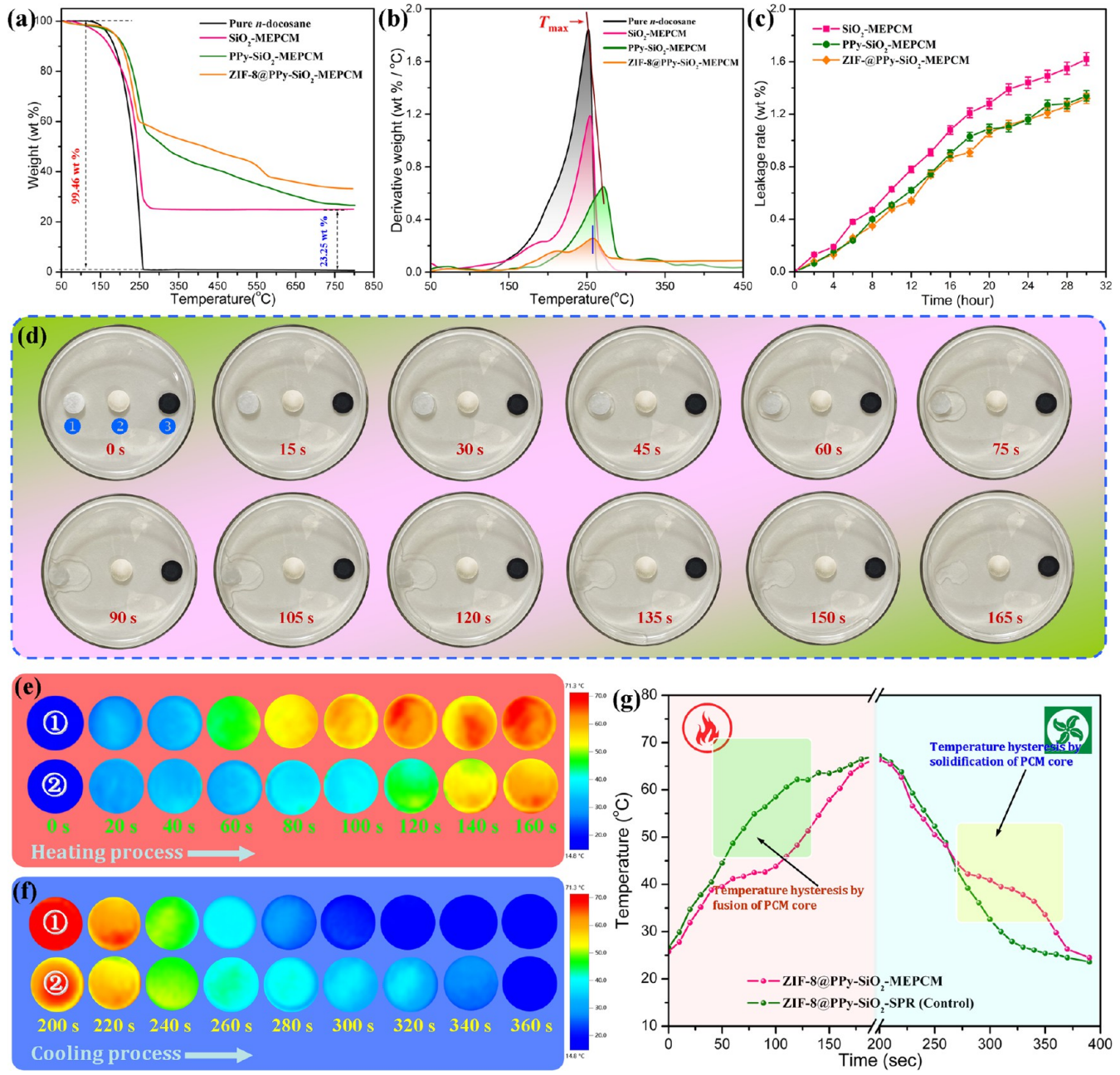

Figure 7. (a) TGA thermograms and (b) DTG curves of pure *n*-docosane and microcapsule samples. (c) Plots of the leakage rate as a function of time for microcapsule samples. (d) Digital photographs of (1) pure *n*-docosane, (2) the SiO_2-MEPCM, and (3) ZIF-8@PPy-SiO_2-MEPCM during the isothermal heating process at 120 °C. Real-time infrared thermographic images of (1) the ZIF-8@PPy-SiO_2-SPR (control) and (2) ZIF-8@PPy-SiO_2-MEPCM recorded in (e) the heating and (f) cooling processes. (g) Plots of temperature evolution as a function of time for the ZIF-8@PPy-SiO_2-MEPCM and ZIF-8@PPy-SiO_2-SPR (control) obtained from infrared thermographic analysis.

enhanced by encapsulating *n*-docosane in silica as a highly thermally conductive inorganic shell. This can enhance the heat transfer and thermal response capability of the microcapsule system. However, a slight reduction in thermal conductance occurs in the PPy-SiO_2-MEPCM and ZIF-8@PPy-SiO_2-MEPCM in comparison with the SiO_2-MEPCM. This was caused by the fabrication of a PPy coating layer and ZIF-8 because these two shell materials have a nature of low thermal conductance. A thermal cycling experiment was carried out to examine the phase-change reversibility and repeatability of the ZIF-8@PPy-SiO_2-MEPCM through 100 cycles of consecutive heating−cooling DSC scans. Figure 6g−i shows the DSC thermograms and corresponding thermal analysis data obtained from every 10 thermal cycles. As seen in Figure 6g, the ZIF-8@PPy-SiO_2-MEPCM exhibits a high coincidence with each other from the first thermal cycle to the last, as shown in its DSC thermograms. Its phase-change enthalpies maintain almost constant quantities with a variation of the thermal cycling number. There is only a small fluctuation in phase-change enthalpy between ±2.2 $J \cdot g^{-1}$ for ΔH_c and between ±2.6 $J \cdot g^{-1}$ for ΔH_m across the whole cycling process, as noted in Figure 6h. All phase-change temperatures were also found to fluctuate slightly within a very narrow range of ± 0.46 °C during the thermal cycling process, as seen in

https://doi.org/10.1021/acsami.1c13446
ACS Appl. Mater. Interfaces 2021, 13, 41753−41772

Figure 6i. FTIR and SEM characterization methods were performed for the ZIF-8@PPy-SiO_2-MEPCM before and after the thermal cycles to evaluate its structural and chemical stabilities over a long-term use for thermal energy storage and release. Figure 6j–l shows the obtained FTIR spectra and SEM images. As seen in Figure 6j, the ZIF-8@PPy-SiO_2-MEPCM exhibits similar intensity and location for the infrared absorption bands in their FTIR spectra before and after 100 thermal cycles. There is no visible difference between the profiles of the two spectra. It is observed from the SEM images in Figure 6k,l that the ZIF-8@PPy-SiO_2-MEPCM shows almost the same morphology before the thermal cycle experiment, indicating its good structural stability. These results clearly prove that the ZIF-8@PPy-SiO_2-MEPCM has a prominent thermal cycling stability to serve for temperature-regulation application in biosensors.

Thermal Management Performance and Working Stability. TGA analysis was conducted to examine the thermal stabilities of three microcapsule samples and pure *n*-docosane as a control, with the resultant TGA thermograms and differential thermogravimetric (DTG) curves displayed in Figure 7a and b, respectively. As observed from the TGA thermograms, pure *n*-docosane presents a typical one-step thermal degradation behavior in the temperature range from 125 to 260 °C with almost no residual char left. This may be attributed to the thermal evaporation of *n*-docosane. The SiO_2-MEPCM also shows a one-step degradation behavior, resulting in a char yield of 23.25 wt %. The residual char is attributed to the indecomposable SiO_2 shell, which is essentially in agreement with the encapsulation ratio of the SiO_2-MEPCM, as listed in Figure 6e. However, the PPy-SiO_2-MEPCM shows a drastic degradation behavior followed by a gradual mass loss in its TGA thermograms, in which the first stage mass loss is attributed to the evaporation of encapsulated *n*-docosane, and the secondary one is due to the high-temperature decomposition of the PPy layer. Furthermore, the ZIF-8@PPy-SiO_2-MEPCM not only shows the same degradation behavior with the PPy-SiO_2-MEPCM but also shows a visible mass loss at around 550 °C. This may result from the decomposition of the crystalline ZIF-8.[40] The characteristic temperature (T_{max}) at maximum mass-loss rate can usually be used as an indication of thermal stability for chemical substances, and it can be obtained from DTG analysis. As observed in Figure 7b, pure *n*-docosane presents a T_{max} at 251 °C, corresponding to its evaporation. In contrast to pure *n*-docosane, there is a slight increase in T_{max} observed from both the SiO_2-MEPCM and the PPy-SiO_2-MEPCM. This may be ascribed to the sealing effect from the SiO_2 shell and PPy layer, which provides an effective protection against the evaporation of the *n*-docosane core. However, the T_{max} of the ZIF-8@PPy-SiO_2-MEPCM was found to decrease slightly. This may be due to the structural damage of the PPy layer with the introduction of ZIF-8. Anyway, the ZIF-8@PPy-SiO_2-MEPCM still exhibits a good thermal stability for thermal management applications.

The antileakage performance of microcapsule samples was evaluated by measuring their leakage rates at different heating times. Figure 7c shows the leakage rates obtained from an accelerated leakage experiment. All microcapsule samples exhibit a gradual decrease in leakage-rate growth with an increase in heating time. Furthermore, the PPy-SiO_2-MEPCM and ZIF-8@PPy-SiO_2-MEPCM exhibit lower leakage rates than the SiO_2-MEPCM at the same heating time, indicating that the fabrication of the PPy coating layer provides an extra protection against the leakage of the *n*-docosane core. It seems that the presence of ZIF-8 on the PPy coating layer does not generate any negative effect on the antileakage performance of microcapsules. The ZIF-8@PPy-SiO_2-MEPCM still exhibits a low leakage rate of 1.32 wt % after heating at 90 °C for 30 h, reflecting an excellent antileakage capability. The high-temperature impact resistance of the ZIF-8@PPy-SiO_2-MEPCM was investigated by means of a high-temperature heat-impact experiment. Figure 7d shows the real-time photographs for the ZIF-8@PPy-SiO_2-MEPCM at different heating times along with pure *n*-docosane and the SiO_2-MEPCM as controls. Pure *n*-docosane was found to lose its original shape easily and flow away as a result of a phase transition from solid to liquid when heated to its melting temperature, suggesting a poor shape stability in the molten state. In contrast, the SiO_2-MEPCM and ZIF-8@PPy-SiO_2-MEPCM always keep their original shape and form without any change across the whole heating process until up to 120 °C for 165 s. There is no leakage observed from two microcapsule samples in the heating process. These phenomena suggest that the fabrication of a SiO_2 shell together with a ZIF-8-anchored PPy coating layer can offer an effective protection against high-temperature impact for the *n*-docosane core, maintaining a good shape/form stability for the ZIF-8@PPy-SiO_2-MEPCM when used at a temperature much higher than the melting point of *n*-docosane.

An infrared thermographic technique was used to characterize the temperature-regulation behavior of the ZIF-8@PPy-SiO_2-MEPCM as well as the ZIF-8@PPy-SiO_2-SPR without an *n*-docosane core as a control. The two microcapsule samples were placed at a hot plate to undergo heating up to 70 °C and then cooled down to room temperature naturally. An infrared thermal imaging camera was used to monitor their surface temperatures in real-time. Figure 7e,f displays the thermographic images of two microcapsule samples recorded during the heating and cooling processes. Meanwhile, Figure 7g shows the plots of surface temperature evolution with of time obtained infrared thermographic analysis. It can be seen in Figure 7e,f that the ZIF-8@PPy-SiO_2-SPR shows a fast color change from blue to green to orange-red in the heating process, but an opposite color evolution during the cooling process. This phenomenon reflects a fast thermal response of the ZIF-8@PPy-SiO_2-SPR without a PCM core. In contrast, the ZIF-8@PPy-SiO_2-MEPCM was found to present a slower change in the surface temperature in the heating and cooling processes (see Figure 7e,f). It is evident that such a delayed thermal response is attributed to the thermal management effect resulting from the PCM core within the ZIF-8@PPy-SiO_2-MEPCM. As observed from the quantitative temperature evolution with time presented in Figure 7g, two visible temperature hysteresis regions can be clearly noted individually in the heating and cooling processes of the ZIF-8@PPy-SiO_2-MEPCM. These two temperature ranges are in good agreement with the melting and crystallization temperature regions of the *n*-docosane core. It is evident that the temperature hysteresis occurring in the ZIF-8@PPy-SiO_2-MEPCM is caused by the latent-heat absorption and release of its *n*-docosane core through melting and crystallization phase transitions. In contrast, the temperature evolution of the ZIF-8@PPy-SiO_2-SPR is only determined from sensible heat due to the absence of a PCM core. As a result, there is no hysteresis appearing in the temperature-evolution plot of the ZIF-8@PPy-SiO_2-SPR, as seen in Figure 7g. The ZIF-8@PPy-SiO_2-

https://doi.org/10.1021/acsami.1c13446
ACS Appl. Mater. Interfaces 2021, 13, 41753–41772

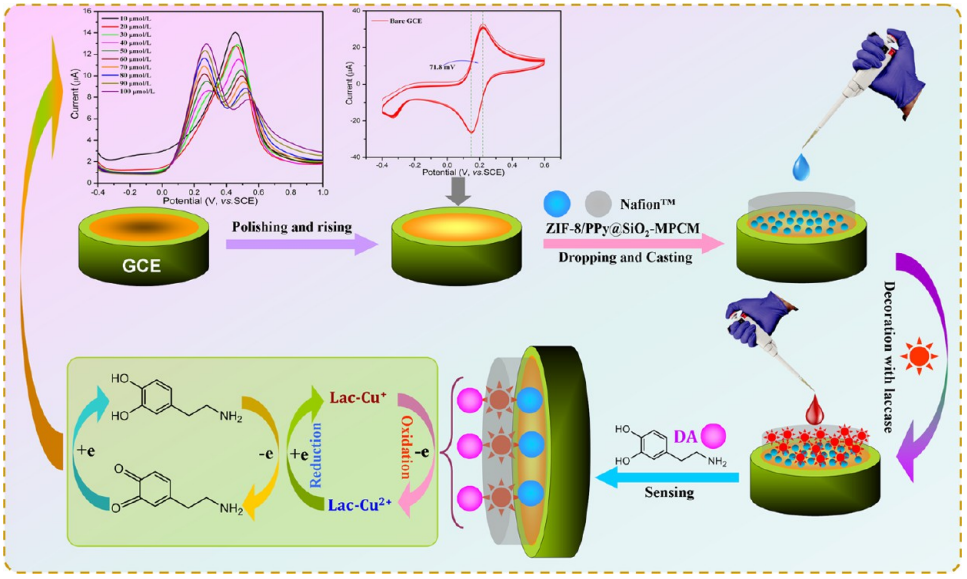

Figure 8. Schematic construction process of an electrochemical biosensor based on the ZIF-8@PPy-SiO_2-MEPCM-modified electrode.

SPR exhibits a rapid thermal response to a change in the background temperature, resulting in a continuous temperature increase or decrease without any discernable hysteresis. These results clearly confirm an effective thermal management capability of the ZIF-8@PPy-SiO_2-MEPCM to conduct temperature regulation to generate a thermal buffering effect *in situ* on its local microenvironment.

Electrochemical Sensing Performance. The electrochemical biosensor based on the ZIF-8@PPy-SiO_2-MEPCM-modified electrode was fabricated with the GCE as a bare electrode by means of the method schematically depicted in Figure 8. CV, EIS, and DPV characterization methods were conducted for the bare GCE and its modified electrodes with different microcapsule samples in a $Fe(CN)_6^{3-/4-}$ solution as a redox probe to confirm the successful construction of an electrochemical biosensor. As shown in Figure 9a, the bare GCE presents a good coincidence in its 10-cycle CV curves, in which two well-defined redox peaks can be clearly observed along with a peak-to-peak separation of around 0.71 V. This indicates that the bare GCE used in this work has a good reversible redox performance and can well serve as a bare electrode for the construction of electrochemical biosensors.[41] Figure 9b displays the Nyquist plots of the bare GCE and its modified electrodes with different microcapsule samples. The performance of these different electrodes with respect to the kinetics of electron transfer can be well reflected from EIS characterization. These Nyquist plots were found to consist of two parts, including a semicircle at high frequencies corresponding to the electron-transfer resistance (R_{ct}) and a linear portion at low frequencies related to the electrochemical behaviors controlled by a diffusion process. It is understandable that the electron-transfer rate is greatly dependent on the R_{ct} value of an electrode because the charges are normally converted on the electrode surface.[42] Both the bare GCE and the SiO_2-MEPCM-modified electrode present a significantly larger semicircle radius than the other electrodes in the high-frequency region in their Nyquist plots, reflecting low electrical conductance. It is notable that the PPy-SiO_2-MEPCM-modified electrode exhibits the smallest semicircle radius among these electrodes, suggesting that this electrode gains enhanced charge transfer in the presence of the conductive PPy coating layer. In contrast to the PPy-SiO_2-MEPCM-modified electrode, the ZIF-8@PPy-SiO_2-MEPCM-modified electrode was found to show an increase in the semicircle radius due to the poor conductive nature of ZIF-8. However, its impedance data show a phase angle larger than 45° in the low frequency. This value is also larger than those of the other modified electrodes, suggesting that the ZIF-8@PPy-SiO_2-MEPCM-modified electrode system has smaller ion-diffusion impedance than the other systems.[43]

CV scanning was carried out for the bare GCE and its modified electrodes with different microcapsule samples in the PBS (0.1 mol·L^{-1}) in the presence and absence of DA as a substrate, with the resultant CV curves presented in Figure 9c,d. It can be seen that there is no redox peak detected on the bare GCE and SiO_2-MEPCM-modified electrode without the substrate, indicating that these two electrodes have no catalytic activity with little detection effectiveness. It should be noted in Figure 9d that a pair of weak redox peaks are observed only from the bare GCE but not from the SiO_2-MEPCM-modified electrode in the presence of DA. This may be due to a weak electrochemical reaction occurring between the conductive surface of the bare electrode and DA. There is a slight enhancement in redox peaks as a result of the presence of a PPy conductive layer in the PPy-SiO_2-MEPCM-modified and ZIF-8@PPy-SiO_2-MEPCM-modified electrodes, as observed in Figure 9c. The ZIF-8@PPy-SiO_2-MEPCM-modified electrode was found to show a pair of well-defined redox peaks in the presence of laccase, even if there is no substrate in the PBS. Such a faradaic behavior is derived from the direct electron transfer between the electrode and the decorated laccase molecules.[44] This suggests that an efficient electronic communication has been established between the bare GCE and the laccase-decorated ZIF-8@PPy layer, leading to a good electrochemical response.[45] It is believable that the ZIF-8@PPy conductive layer plays an important role in promoting the electron exchange between the bare GCE and the electroactive center of laccase.[46] Therefore, a superior electrocatalytic activity of laccase can be achieved for DA with the aid of the ZIF-8@PPy layer. The ZIF-8@PPy-SiO_2-MEPCM-modified electrode presents a further enhancement in redox peak current in the presence of DA, as seen in Figure 9d. Such a pair

https://doi.org/10.1021/acsami.1c13446
ACS Appl. Mater. Interfaces 2021, 13, 41753−41772

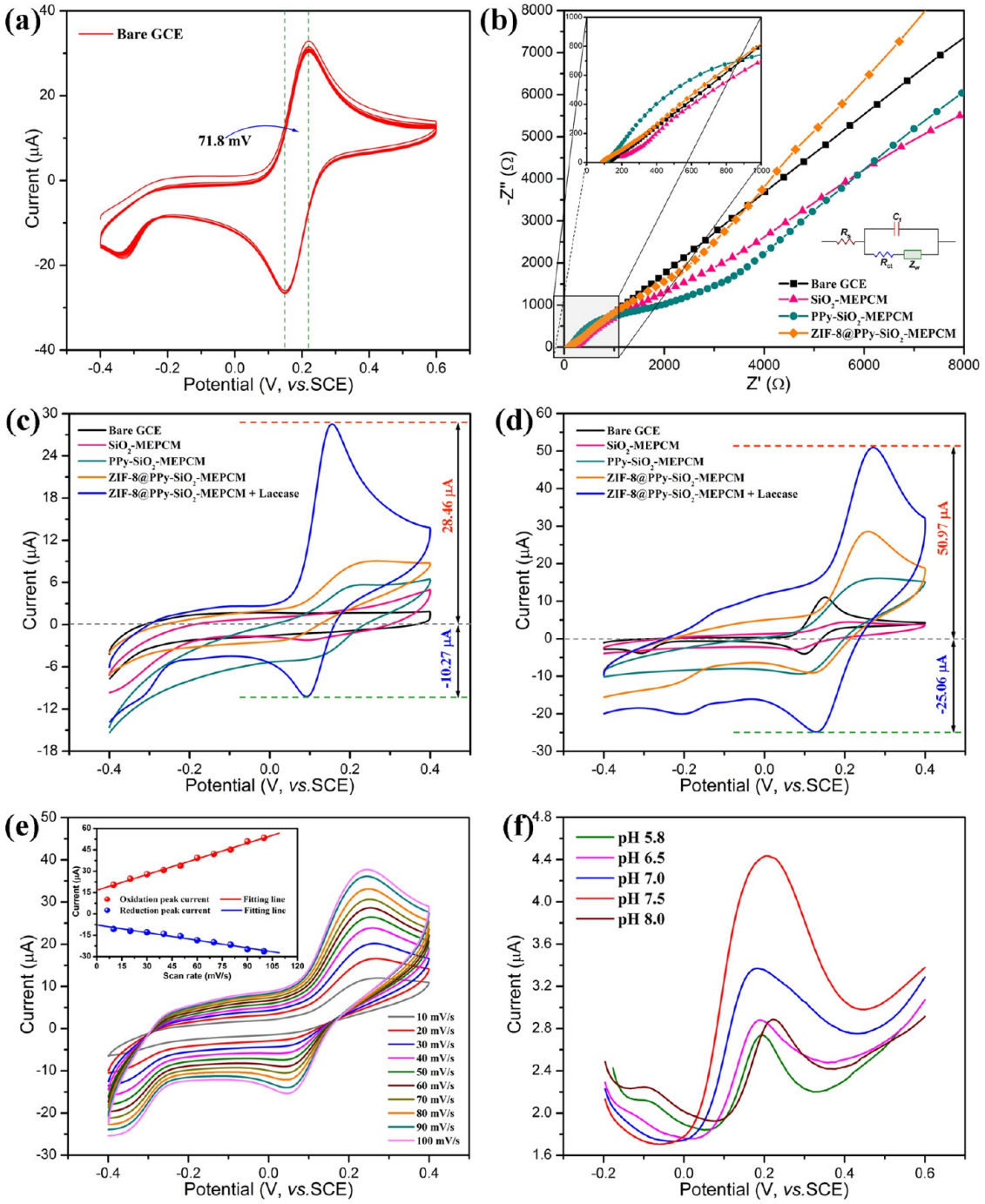

Figure 9. (a) Cyclic CV cures of the bare GCE. (b) Nyquist plots of the bare GCE and its modified electrode with different microcapsule samples. CV curves of the bare GCE and its modified electrode with different microcapsule samples (c) without DA (substrate) and (d) with DA. (e) CV curves of the ZIF-8@PPy-SiO_2-MEPCM-modified electrode at different scan rates. (f) Effects of pH on the DPV behaviors of the electrochemical biosensor based on the ZIF-8@PPy-SiO_2-MEPCM-modified electrode.

of well-defined redox peaks with enhanced peak currents can be assigned to the oxidation of DA to dopamine quinone and the subsequent reduction of dopamine quinone to DA, as reported in the literature.[47] The electrochemical behavior of the ZIF-8@PPy-SiO_2-SPR-modified electrode was also characterized with CV in the presence and absence of DA, with the resultant CV curves presented in Figure S1 (see the Supporting Information). Similar to the ZIF-8@PPy-SiO_2-MEPCM-modified electrode, there is a significant enhancement in redox peaks observed in the ZIF-8@PPy-SiO_2-SPR-modified electrode in the presence of DA, indicating that this modified electrode has a clear electrochemical response to DA and can be used as a qualified control for further comparative study.

According to the electrochemical catalytic mechanism depicted in Figure 8, DA is first oxidized to dopamine-*o*-quinone by the laccase (Lac-Cu^{2+}), and then the laccase loses electrons to form the laccase (Lac-Cu^{+}). Such redox reactions lead to a bioelectrocatalytic cycle, consequently generating electrons to be transferred to the working electrode. In this electrochemical biosensing system, ZIF-8 possesses a large

https://doi.org/10.1021/acsami.1c13446
ACS Appl. Mater. Interfaces 2021, 13, 41753−41772

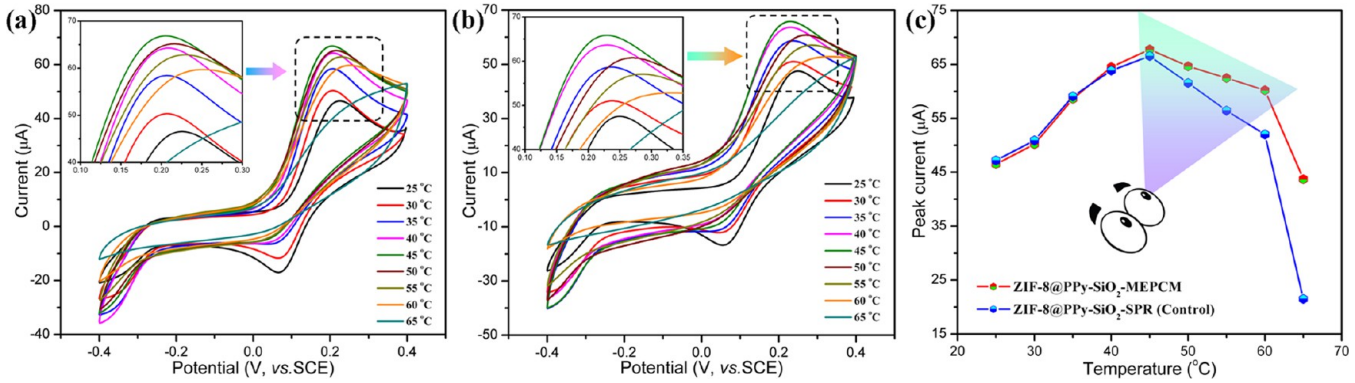

Figure 10. CV curves of (a) the ZIF-8@PPy-SiO_2-MEPCM-modified and (b) ZIF-8@PPy-SiO_2-SPR-modified electrodes at different ambient temperatures. (c) Plots of oxidation peak current as a function of ambient temperature for the ZIF-8@PPy-SiO_2-MEPCM and ZIF-8@PPy-SiO_2-SPR-modified electrodes.

specific surface area and, therefore, can provide a great number of catalytic active sites for the electrochemical reaction of DA, resulting in an enhancement in the electrochemical response. Moreover, the presence of PPy as a conductive polymer can greatly enhance the redox peak responses under the rapid electron transfer. The effect of the scan rate on the electrochemical behavior of the biosensor constructed with the ZIF-8@PPy-SiO_2-MEPCM-modified electrode was evaluated by CV. Figure 9e presents the CV curves obtained at different scan rates alone with the data of redox peak currents. There is a good linear relation between the redox peak currents and the scan rate. This indicates that an adsorption-controlled electron process dominates the electron transfer in this biosensing system.[48] Furthermore, such an electron-transfer process is rapid and quasi-reversible, as observed from the CV curves in Figure 9e, suggesting that the biosensing system facilitates a facile electron-transfer reaction. These results demonstrate that the electrochemical biosensor fabricated in this study has a good electrochemical response together with a high biocatalytic activity for the detection of DA. In addition, DPV characterization was performed to evaluate the effect of pH on the electrochemical behavior of the fabricated biosensor for DA detection. Figure 9f shows the DPV curves obtained in the range of pH 5.8−8.0. These DPV curves exhibit a significant change in peak current with a variation of pH. It is noticeable that a maximum oxidation peak current is achieved for the biosensor at pH 7.5, which may be associated with the protons involved in the electrochemical reactions. Therefore, pH ∼ 7.5 is considered as a desirable pH value for future experiments.

Effect of Temperature on Biosensing Detection of DA. It is expected for us to make an intelligent combination of the PCM and electroactive substance through the fabrication of the ZIF-8@PPy-SiO_2-MEPCM. As a result of this integration, the resultant electrochemical biosensor can obtain a thermal self-regulation capability to generate a thermal buffering effect *in situ* on its microenvironment under a drastic fluctuation of ambient temperature. This can be realized through phase transitions of the PCM core of the ZIF-8@PPy-SiO_2-MEPCM in the working electrode. To identify the thermal self-regulation effectiveness of the ZIF-8@PPy-SiO_2-MEPCM in the electrochemical biosensor, CV and DPV characterization methods were performed for the ZIF-8@PPy-SiO_2-MEPCM-modified electrodes at different ambient temperatures, and the ZIF-8@PPy-SiO_2-SPR-modified electrode without a PCM inside was examined as a control electrode. Figure 10a,b shows the CV curves of the ZIF-8@PPy-SiO_2-MEPCM-modified and ZIF-8@PPy-SiO_2-SPR-modified electrodes at different ambient temperatures, respectively. These two modified electrodes exhibit an increasing trend in oxidation peak current as the ambient temperature increases up to 45 °C. This phenomenon indicates that the electrochemical biosensors have an increasing biocatalytic activity to DA with an increase in temperature. The oxidation peak currents of the two modified electrodes decrease with a continuous increase in ambient temperature, indicating that the biocatalytic activity of laccase tends to deteriorate at higher temperatures. It is concluded that the electrochemical biosensors constructed in this work can achieve a maximum biocatalytic activity at an optimal temperature of 45 °C. However, it is of interest to note that the ZIF-8@PPy-SiO_2-MEPCM-modified electrode presents a slower decreasing trend in oxidation peak current than the control electrode with a further increase in ambient temperature. Such a trend can also be clearly observed from the plots of oxidation peak current as a function of ambient temperature for the ZIF-8@PPy-SiO_2-MEPCM modified and control electrodes in Figure 10c. This may be due to the fact that the *n*-docosane core in the ZIF-8@PPy-SiO_2-MEPCM can generate a cooling effect *in situ* on its modified electrode through latent-heat absorption in the melting process. As a result of the cooling effect, the microenvironmental temperature around the working electrode tends to decrease at any ambient temperatures higher than 45 °C. This evidently depresses the deterioration of biocatalytic activity of laccase and enhances the electrochemical response to DA accordingly. In contrast, there is no cooling effect generated in the ZIF-8@PPy-SiO_2-SPR-modified electrode due to the absence of the PCM core. This leads to a continuous deterioration of biocatalytic activity of the resultant biosensor at an ambient temperature higher than 45 °C, and therefore the ZIF-8@PPy-SiO_2-SPR-modified electrode presents a rapid reduction in oxidation peak current than the ZIF-8@PPy-SiO_2-MEPCM-modified one as seen in Figure 10c.

DPV has been recognized to be a valuable technique in many ways complementary to CV. Based on this technique, a fast, sensitive, reliable, and high-resolution detection effect can be achieved for analytes in electrochemical sensing systems due to its intrinsic high current sensitivity and low charging contribution to the background current.[49] To further confirm

https://doi.org/10.1021/acsami.1c13446
ACS Appl. Mater. Interfaces 2021, 13, 41753−41772

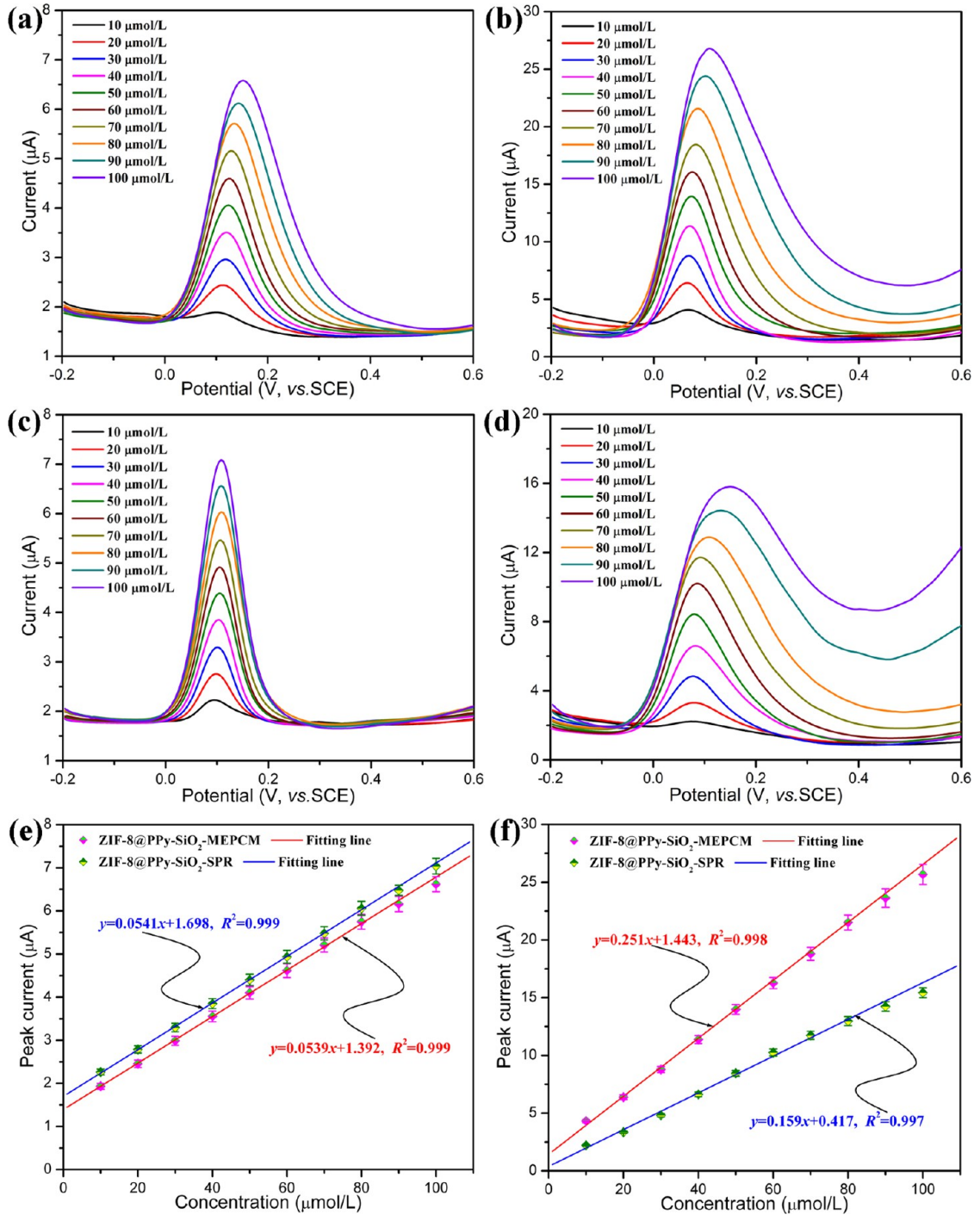

Figure 11. DPV curves of the ZIF-8@PPy-SiO_2-MEPCM-modified electrode at (a) 25 °C and (b) 50 °C. DPV curves of the ZIF-8@PPy-SiO_2-SPR-modified electrode at (c) 25 °C and (d) 50 °C. Plots of oxidation peak current as a function of DA concentration and corresponding linear fits for the biosensors at (e) 25 °C and (f) 50 °C.

the thermal self-regulation effect existing in the electrochemical biosensor based on the ZIF-8@PPy-SiO_2-MEPCM-modified electrode, DPV measurements were performed at 25 and 50 °C for the corresponding biosensor at different concentrations of DA ranging from 10.0 to 100.0 $\mu mol \cdot L^{-1}$. Meanwhile, the ZIF-8@PPy-SiO_2-SPR-modified electrode without a PCM inside was also examined as a control electrode by DPV under identical conditions. The resultant DPV curves are presented in Figure 11a–d. It can be seen that both of the modified electrodes present an increase in oxidation peak current with increasing the concentration of DA at 25 and 50 °C in the PBS (0.1 $\mu mol \cdot L^{-1}$, pH ~ 7.4). The oxidation peak current at 50 °C was found to be much greater than that at 25 °C when the two modified electrodes were used to detect DA at the same concentration. It is understandable that a higher temperature can improve the electron-transfer rate in the biosensing system and promotes redox reactions accordingly. Consequently, the electrochemical response was enhanced significantly.[50] It is worth noting in Figure 11e,f that there is a good linear relationship between the oxidation peak current

https://doi.org/10.1021/acsami.1c13446
ACS Appl. Mater. Interfaces 2021, 13, 41753–41772

Table 1. Linear Regression Equations, Sensitivities, and Limits of Detection of the Biosensors at Different Ambient Temperatures

biosensor type	temperature (°C)	linear regression equation	R^2	sensitivity ($\mu A \cdot L \cdot \mu mol^{-1} \cdot cm^{-2}$)	limit of detection ($\mu mol \cdot L^{-1}$)
the biosensor based on the ZIF-8@PPy-SiO_2-MEPCM	25	$I_{pa} = 0.539 \cdot c_{DA} + 1.392$	0.999	0.758 ± 0.01	0.0321 ± 0.001
	50	$I_{pa} = 0.251 \cdot c_{DA} + 1.443$	0.998	3.541 ± 0.03	0.0069 ± 0.001
the biosensor based on the ZIF-8@PPy-SiO_2-SPR	25	$I_{pa} = 0.541 \cdot c_{DA} + 1.698$	0.999	0.766 ± 0.01	0.0322 ± 0.001
	50	$I_{pa} = 0.159 \cdot c_{DA} + 0.417$	0.997	2.211 ± 0.02	0.0109 ± 0.001

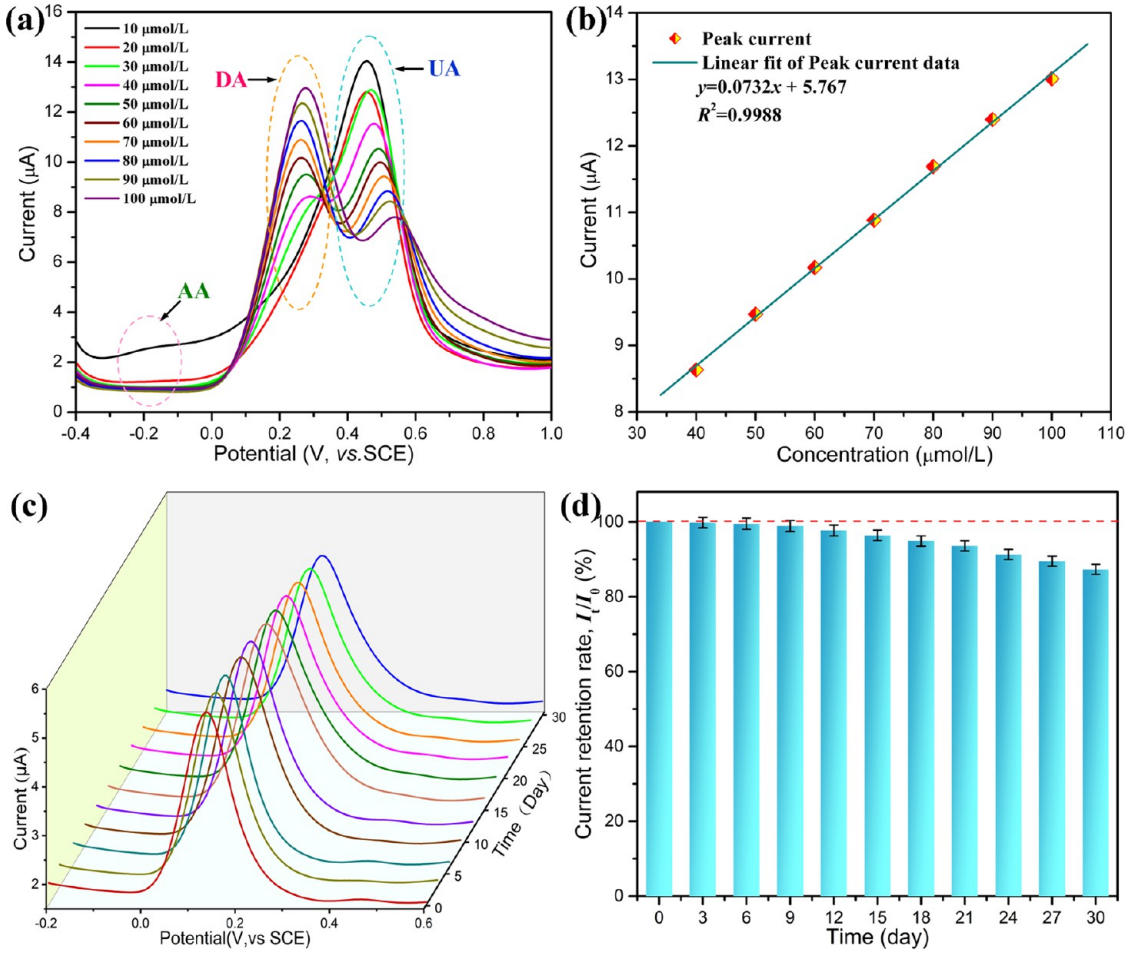

Figure 12. (a) DPV curves of the biosensor based on the ZIF-8@PPy-SiO_2-MEPCM-modified electrode with mixed solutions of DA, AA, and UA at different concentrations of DA and fixed concentrations of AA (1.0 mmol·L^{-1}) and UA (200.0 μmol·L^{-1}). (b) Plot of oxidation peak current as a function of DA concentration along with the corresponding linear fit for the biosensor based on the ZIF-8@PPy-SiO_2-MEPCM-modified electrode. (c) DPV curves of the biosensor based on the ZIF-8@PPy-SiO_2-MEPCM-modified electrode with a DA concentration of 100.0 μmol·L^{-1} after storage for different days. (d) Plots of oxidation peak current as a function of storage day for the biosensor based on the ZIF-8@PPy-SiO_2-MEPCM-modified electrode.

(I_{pa}, μmol·L^{-1}) and DA concentration (c_{DA}, μmol·L^{-1}), indicating a good linear response for the two modified electrodes in the DA concentration range of 10.0−100.0 μmol·L^{-1} at two different temperatures. The linear regression equations of two modified electrodes at 25 and 50 °C were determined according to the linear fits and then presented in Table 1. Furthermore, their sensitivities can be calculated according to the ratio of the slope of the fit line to the surface area of the electrode. Their limits of detection can be determined in terms of the signal-to-noise ratio of 3 (S/N = 3) using the formula of $3s/b$, where s and b represent the relative standard deviation (RSD) of a blank solution and sensitivity, respectively. These important biosensing data are also summarized in Table 1. Based on the results in Table 1, the biosensor based on the ZIF-8@PPy-SiO_2-MEPCM-modified electrode was found to exhibit a sensitivity and limit of detection similar to the biosensor using the control electrode when detecting DA at 25 °C. However, it presents a higher sensitivity to DA together with a lower limit of detection than the control biosensor at a detection temperature of 50 °C. Evidently, the ZIF-8@PPy-SiO_2-MEPCM-modified electrode presents a better biocatalytic effect on DA at a higher temperature than the ZIF-8@PPy-SiO_2-SPR-modified one as a result of the thermal self-regulation effect derived from the integration of PCM and the electrode. This result is also in good agreement with those obtained from CV measurements. In conclusion, the biosensor developed in this work has a stronger determination capability and better

https://doi.org/10.1021/acsami.1c13446
ACS Appl. Mater. Interfaces 2021, 13, 41753−41772

detection effectiveness toward DA at a higher ambient temperature than the conventional ones.

Anti-interferential Performance and Storage Stability. The anti-interference capability of the biosensor based on the ZIF-8@PPy-SiO_2-MEPCM-modified electrode was investigated by DPV using UA and AA as interfering substances against DA because these two potential interfering molecules exist in biological environments together with DA in most cases.[51] DPV measurements were conducted at room temperature using a series of solutions with different concentrations of DA and fixed concentrations of UA and AA, with the resultant DPV curves presented in Figure 12a. It can be seen that DA and UA exhibit two separated oxidation peaks at different potentials in the ranges of 0.276−0.288 and 0.455−0.541 V, respectively. However, there is no electrochemical signal observed from AA, indicating an extremely weak electrochemical response to AA in this biosensor. Although the biosensor based on the ZIF-8@PPy-SiO_2-MEPCM-modified electrode presents a sensitive electrochemical response to DA and UA as observed from its DPV curves, there are different variation trends in oxidation peak currents related to DA and UA with an increase in the concentration of DA. The oxidation peak current corresponding to DA increases significantly with an increase in the DA concentration, whereas the oxidation peak current of UA was found to drop remarkably. This indicates that there is no significant influence on the biosensing identification of DA in the presence of interfering molecules, UA and AA. Moreover, it can also be observed in Figure 12b that the oxidation peak current presents a good linear electrochemical response to DA at a concentration ranging from 40.0 to 90.0 $\mu mol \cdot L^{-1}$. The sensitivity and limit of detection were determined to be 1.034 ± 0.02 $\mu A \cdot L \cdot \mu mol^{-1} \cdot cm^{-2}$ and 0.024 ± 0.02 $\mu mol \cdot L^{-1}$, respectively. These results suggest that DA can be allowed to be determined selectively in this biosensing system even if there are other interfering substances existing in the analyte specimen. The storage stability of the biosensor based on the ZIF-8@PPy-SiO_2-MEPCM-modified electrode was evaluated by DPV after the modified electrode was stored in the PBS at 4 °C for 30 days. The DPV response of the biosensor to a DA solution (100.0 $\mu mol \cdot L^{-1}$) was examined intermittently every 3 days, with the resultant DPV curves presented in Figure 12c. There is no evident change in oxidation peak current observed from these DPV curves after the modified electrode was stored for 30 days. Figure 12d shows the retention rate of oxidation peak current as a function of storage day for the biosensor. It can be seen that the biosensor only lost 3.6% of oxidation peak current after storage for 15 days. It is of importance to note that the DPV current response still retained 87.3% of its original response after storage for 30 days, reflecting a satisfactory storage stability of the biosensor developed in this work.

CONCLUSIONS

In this work, the ZIF-8@PPy-SiO_2-MEPCM has been fabricated by microencapsulating an *n*-docosane core in the SiO_2 shell *via* emulsion-templated interfacial polycondensation, followed by depositing a ZIF-8-anchored PPy layer as an electroactive substance on the surface of the SiO_2 shell through surfactant-assisted oxidation polymerization. The obtained microcapsules present a well-defined core−shell microstructure, a regular spherical morphology, and a uniform particle size, together with the desired chemical compositions and structures. The ZIF-8@PPy-SiO_2-MEPCM not only reveals a good thermal management capability to carry out temperature regulation under a latent-heat capacity of around 124.0 $J \cdot g^{-1}$ but also exhibits an excellent thermal cycling stability and good thermal impact resistance in long-term use for temperature regulation and thermal management. All of these were considered to indicate the successful formation of the ZIF-8@PPy-SiO_2-MEPCM in terms of our design strategy and aim. A novel electrochemical biosensing system was designed and constructed with the ZIF-8@PPy-SiO_2-MEPCM-modified electrode to achieve a thermal self-regulation function for enhancing the biosensing detection of DA under thermal management. The biosensor exhibits stronger determination capability and better detection effectiveness for DA at a higher ambient temperature than conventional biosensors thanks to the *in situ* thermal management derived from the integration of phase-change microcapsules and their ZIF-8@PPy electroactive layer. In addition, the biosensor demonstrates a good anti-interferential capability, high selectivity, and satisfactory storage stability for the detection and determination of DA in practical applications. This study provides a promising approach for the design and development of intelligent thermal self-regulatory biosensors with an enhanced detection capability in a wide range of applicable temperatures.

ASSOCIATED CONTENT

Supporting Information

The Supporting Information is available free of charge at https://pubs.acs.org/doi/10.1021/acsami.1c13446.

CV curves of the ZIF-8@PPy-SiO_2-SPR-modified electrodes in the presence and absence of DA as a substrate; table for the comparison of thermal performance of the microcapsule samples synthesized in this work and other microencapsulated paraffin-type PCMs with various SiO_2-based shells reported in the literature (PDF)

AUTHOR INFORMATION

Corresponding Authors

Huan Liu − *State Key Laboratory of Organic−Inorganic Composites, Beijing University of Chemical Technology, Beijing 100029, P. R. China*; Email: bucthuan@163.com

Xiaodong Wang − *State Key Laboratory of Organic−Inorganic Composites, Beijing University of Chemical Technology, Beijing 100029, P. R. China*; orcid.org/0000-0002-8787-1268; Email: wangxdfox@aliyun.com

Authors

Jingjing Li − *State Key Laboratory of Organic−Inorganic Composites, Beijing University of Chemical Technology, Beijing 100029, P. R. China*

Jinghua Yu − *State Key Laboratory of Organic−Inorganic Composites, Beijing University of Chemical Technology, Beijing 100029, P. R. China*

Zhao Sun − *State Key Laboratory of Organic−Inorganic Composites, Beijing University of Chemical Technology, Beijing 100029, P. R. China*

Complete contact information is available at: https://pubs.acs.org/10.1021/acsami.1c13446

Notes

The authors declare no competing financial interest.

■ ACKNOWLEDGMENTS

This work was supported by the National Natural Science Foundation of China (Grant Nos. 51873010 and 51903010).

■ REFERENCES

(1) Alehosseini, E.; Jafari, S. M. Nanoencapsulation of Phase Change Materials (Pcms) and Their Applications in Various Fields for Energy Storage and Management. *Adv. Colloid Interface Sci.* **2020**, *283*, No. 102226.
(2) Liu, Z.; Hu, Q.; Guo, S.; Yu, L.; Hu, X. Thermoregulating Separators Based on Phase-Change Materials for Safe Lithium-Ion Batteries. *Adv. Mater.* **2021**, *33*, No. 2008088.
(3) Chen, X.; Gao, H.; Tang, Z.; Dong, W.; Li, A.; Wang, G. Optimization Strategies of Composite Phase Change Materials for Thermal Energy Storage, Transfer, Conversion and Utilization. *Energy Environ. Sci.* **2020**, *13*, 4498−4535.
(4) Yuan, K.; Shi, J.; Aftab, W.; Qin, M.; Usman, A.; Zhou, F.; Lv, Y.; Gao, S.; Zou, R. Engineering the Thermal Conductivity of Functional Phase-Change Materials for Heat Energy Conversion, Storage, and Utilization. *Adv. Funct. Mater.* **2020**, *30*, No. 1904228.
(5) Zhang, N.; Yuan, Y.; Cao, X.; Du, Y.; Zhang, Z.; Gui, Y. Latent Heat Thermal Energy Storage Systems with Solid−Liquid Phase Change Materials: A Review. *Adv. Eng. Mater.* **2018**, *20*, No. 1700753.
(6) Ran, F.; Chen, Y.; Cong, R.; Fang, G. Flow and Heat Transfer Characteristics of Microencapsulated Phase Change Slurry in Thermal Energy Systems: A Review. *Renewable Sustainable Energy Rev.* **2020**, *134*, No. 110101.
(7) Yang, L.; Liu, S.; Zheng, H. A Comprehensive Review of Hydrodynamic Mechanisms and Heat Transfer Characteristics for Microencapsulated Phase Change Slurry (MPCS) in Circular Tube. *Renewable Sustainable Energy Rev.* **2019**, *114*, No. 109312.
(8) Wang, W.; Cai, Y.; Du, M.; Hou, X.; Liu, J.; Ke, H.; Wei, Q. Ultralight and Flexible Carbon Foam-Based Phase Change Composites with High Latent-Heat Capacity and Photothermal Conversion Capability. *ACS Appl. Mater. Interfaces* **2019**, *11*, 31997−32007.
(9) Seitz, S.; Ajiro, H. Self-Assembling Weak Polyelectrolytes for the Layer-by-Layer Encapsulation of Paraffin-Type Phase Change Material Icosane. *Sol. Energy Mater. Sol. Cells* **2019**, *190*, 57−64.
(10) Döğüşcü, D. K.; Damlıoğlu, Y.; Alkan, C. Poly(Styrene-Co-Divinylbenzene-Co-Acrylamide)/N-octadecane Microencapsulated Phase Change Materials for Thermal Energy Storage. *Sol. Energy Mater. Sol. Cells* **2019**, *198*, 5−10.
(11) Liu, C.; Rao, Z.; Zhao, J.; Huo, Y.; Li, Y. Review on Nanoencapsulated Phase Change Materials: Preparation, Characterization and Heat Transfer Enhancement. *Nano Energy* **2015**, *13*, 814−826.
(12) Zhang, Y.; Jiang, Z.; Zhang, Z.; Ding, Y.; Yu, Q.; Li, Y. Polysaccharide Assisted Microencapsulation for Volatile Phase Change Materials with a Fluorescent Retention Indicator. *Chem. Eng. J.* **2019**, *359*, 1234−1243.
(13) Liu, H.; Wang, X. D.; Wu, D. Z. Innovative Design of Microencapsulated Phase Change Materials for Thermal Energy Storage and Versatile Applications: A Review. *Sustainable Energy Fuels* **2019**, *3*, 1091−1149.
(14) Chen, X.; Tang, Z.; Liu, P.; Gao, H.; Chang, Y.; Wang, G. Smart Utilization of Multifunctional Metal Oxides in Phase Change Materials. *Matter* **2020**, *3*, 708−741.
(15) Chen, L.; Wu, Z.-Q.; Wang, C.; Ouyang, J.; Xia, X.-H. Exploring the Temperature-Dependent Kinetics and Thermodynamics of Immobilized Glucose Oxidase in Microchip. *Anal. Methods* **2012**, *4*, 2831−2837.
(16) Huang, Y.; Li, H.; Wang, Z.; Zhu, M.; Pei, Z.; Xue, Q.; Huang, Y.; Zhi, C. Nanostructured Polypyrrole as a Flexible Electrode Material of Supercapacitor. *Nano Energy* **2016**, *22*, 422−438.
(17) Wu, S. H.; Huang, X. B.; Tang, Y.; Ma, L. M.; Liu, Y.; Sun, J. J. Temperature Controllable Electrochemical Sensors Based on Horseradish Peroxidase as Electrocatalyst at Heated Au Disk Electrode and Its Preliminary Application for H_2O_2 Detection. *Anal. Chim. Acta* **2020**, *1096*, 44−52.
(18) Xu, X.-y.; Liu, J.-h.; Ouyang, X.; Cui, L.; Hong, J.; Meng, X.; Qin, S.; Liu, C.; Tang, J.; Chen, D.-Z. In-Situ Temperature Regulation of Flexible Supercapacitors by Designing Intelligent Electrode with Microencapsulated Phase Change Materials. *Electrochim. Acta* **2020**, *334*, No. 135551.
(19) Li, J. D.; Liu, H.; Wang, X. D.; Wu, D. Z. Development of Thermoregulatory Enzyme Carriers Based on Microencapsulated *N*-docosane Phase Change Material for Biocatalytic Enhancement of Amylases. *ACS Sustainable Chem. Eng.* **2017**, *5*, 8396−8406.
(20) Jiang, B. B.; Wang, X. D.; Wu, D. Z. Fabrication of Microencapsulated Phase Change Materials with TiO_2 /Fe_3O_4 Hybrid Shell as Thermoregulatory Enzyme Carriers: A Novel Design of Applied Energy Microsystem for Bioapplications. *Appl. Energy* **2017**, *201*, 20−33.
(21) Cao, P.; Liu, H.; Wu, D.; Wang, X. Immobilization of Laccase on Phase-Change Microcapsules as Self-Thermoregulatory Enzyme Carrier for Biocatalytic Enhancement. *Chem. Eng. J.* **2021**, *405*, No. 126695.
(22) Xu, Q.; Liu, H.; Wang, X. D.; Wu, D. Z. Smart Design and Construction of Nanoflake-Like MnO_2/SiO_2 Hierarchical Microcapsules Containing Phase Change Material for in-Situ Thermal Management of Supercapacitors. *Energy Convers. Manage.* **2018**, *164*, 311−328.
(23) Sun, Z.; Zhao, L. J.; Wan, H. X.; Liu, H.; Wu, D. Z.; Wang, X. D. Construction of Polyaniline/Carbon Nanotubes-Functionalized Phase-Change Microcapsules for Thermal Management Application of Supercapacitors. *Chem. Eng. J.* **2020**, *396*, No. 125317.
(24) Sajid, M.; Baig, N.; Alhooshani, K. Chemically Modified Electrodes for Electrochemical Detection of Dopamine: Challenges and Opportunities. *TrAC, Trends Anal. Chem.* **2019**, *118*, 368−385.
(25) Shao, K.; You, J.; Ye, S.; Gu, D.; Wang, T.; Teng, Y.; Shen, Z.; Pan, Z. Gold Nanoclusters-Poly(9,9-Dioctylfluorenyl-2,7-Diyl) Dots@Zeolitic Imidazolate Framework-8 (ZIF-8) Nanohybrid Based Probe for Ratiometric Analysis of Dopamine. *Anal. Chim. Acta* **2020**, *1098*, 102−109.
(26) Rodríguez-Delgado, M. M.; Alemán-Nava, G. S.; Rodríguez-Delgado, J. M.; Dieck-Assad, G.; Martínez-Chapa, S. O.; Barceló, D.; Parra, R. Laccase-Based Biosensors for Detection of Phenolic Compounds. *TrAC, Trends Anal. Chem.* **2015**, *74*, 21−45.
(27) Jiang, L.; Nelson, G. W.; Abda, J.; Foord, J. S. Novel Modifications to Carbon-Based Electrodes to Improve the Electrochemical Detection of Dopamine. *ACS Appl. Mater. Interfaces* **2016**, *8*, 28338−28348.
(28) Miralles, V.; Huerre, A.; Malloggi, F.; Jullien, M. C. A Review of Heating and Temperature Control in Microfluidic Systems: Techniques and Applications. *Diagnostics* **2013**, *3*, 33−67.
(29) Lin, C.; Du, Y.; Wang, S.; Wang, L.; Song, Y. Glucose Oxidase@Cu-Hemin Metal-Organic Framework for Colorimetric Analysis of Glucose. *Mater. Sci. Eng., C* **2021**, *118*, No. 111511.
(30) Li, K.; Kang, J.; Zhan, T.; Cao, W.; Liu, X.; Gao, H.; Si, C.; She, X. Electrochemical Sensing Platform for Naphthol Isomers Based on in Situ Growth of ZIF-8 on Reduced Graphene Oxide by a Reaction-Diffusion Technique. *J. Colloid Interface Sci.* **2021**, *581*, 576−585.
(31) Jain, R.; Jadon, N.; Pawaiya, A. Polypyrrole Based Next Generation Electrochemical Sensors and Biosensors: A Review. *TrAC, Trends Anal. Chem.* **2017**, *97*, 363−373.
(32) Liu, H.; Qian, Z.; Wang, Q.; Wu, D.; Wang, X. Development of Renewable Biomass-Derived Carbonaceous Aerogel/Mannitol Phase-Change Composites for High Thermal-Energy-Release Efficiency and Shape Stabilization. *ACS Appl. Energy Mater.* **2021**, *4*, 1714−1730.
(33) Xu, X.; Tang, J.; Qian, H.; Hou, S.; Bando, Y.; Hossain, M. S. A.; Pan, L.; Yamauchi, Y. Three-Dimensional Networked Metal-Organic Frameworks with Conductive Polypyrrole Tubes for Flexible Supercapacitors. *ACS Appl. Mater. Interfaces* **2017**, *9*, 38737−38744.

https://doi.org/10.1021/acsami.1c13446
ACS Appl. Mater. Interfaces 2021, 13, 41753−41772

(34) González-Casamachin, D. A.; Rivera De la Rosa, J.; Lucio-Ortiz, C. J.; De Haro De Rio, D. A.; Martínez-Vargas, D. X.; Flores-Escamilla, G. A.; Dávila Guzman, N. E.; Ovando-Medina, V. M.; Moctezuma-Velazquez, E. Visible-Light Photocatalytic Degradation of Acid Violet 7 Dye in a Continuous Annular Reactor Using ZnO/Ppy Photocatalyst: Synthesis, Characterization, Mass Transfer Effect Evaluation and Kinetic Analysis. *Chem. Eng. J.* **2019**, *373*, 325−337.
(35) Chan, D. H.; Millet, A.; Fisher, C. R.; Price, M. C.; Burchell, M. J.; Armes, S. P. Synthesis and Characterization of Polypyrrole-Coated Anthracene Microparticles: A New Synthetic Mimic for Polyaromatic Hydrocarbon-Based Cosmic Dust. *ACS Appl. Mater. Interfaces* **2021**, *13*, 3175−3185.
(36) Tran, T. V.; Nguyen, H.; Le, P. H. A.; Nguyen, D. T. C.; Nguyen, T. T.; Nguyen, C. V.; Vo, D.-V. N.; Nguyen, T. D. Microwave-Assisted Solvothermal Fabrication of Hybrid Zeolitic−Imidazolate Framework (ZIF-8) for Optimizing Dyes Adsorption Efficiency Using Response Surface Methodology. *J. Environ. Chem. Eng.* **2020**, *8*, No. 104189.
(37) Rafti, M.; Marmisollé, W. A.; Azzaroni, O. Metal-Organic Frameworks Help Conducting Polymers Optimize the Efficiency of the Oxygen Reduction Reaction in Neutral Solutions. *Adv. Mater. Interfaces* **2016**, *3*, No. 1600047.
(38) Di Giambattista, C.; Sanctuary, R.; Perigo, E.; Baller, J. Relaxations in the Metastable Rotator Phase of N-Eicosane. *J. Chem. Phys.* **2015**, *143*, No. 054507.
(39) Su, Y. L.; Liu, G. M.; Xie, B. Q.; Fu, D. S.; Wang, D. J. Crystallization Features of Normal Alkanes in Confined Geometry. *Acc. Chem. Res.* **2014**, *47*, 192−201.
(40) Sasikumar, B.; Bisht, S.; Arthanareeswaran, G.; Ismail, A. F.; Othman, M. H. D. Performance of Polysulfone Hollow Fiber Membranes Encompassing ZIF-8, SiO_2/ZIF-8, and Amine-Modified SiO_2/ZIF-8 Nanofillers for CO_2/CH_4 and CO_2/N_2 Gas Separation. *Sep. Purif. Technol.* **2021**, *264*, No. 118471.
(41) Tang, W.; Li, L.; Zeng, X. A Glucose Biosensor Based on the Synergistic Action of Nanometer-Sized TiO_2 and Polyaniline. *Talanta* **2015**, *131*, 417−423.
(42) Iranmanesh, T.; Foroughi, M. M.; Jahani, S.; Shahidi Zandi, M.; Hassani Nadiki, H. Green and Facile Microwave Solvent-Free Synthesis of CeO_2 Nanoparticle-Decorated Cnts as a Quadruplet Electrochemical Platform for Ultrasensitive and Simultaneous Detection of Ascorbic Acid, Dopamine, Uric Acid and Acetaminophen. *Talanta* **2020**, *207*, No. 120318.
(43) Zhang, W.; Duan, D.; Liu, S.; Zhang, Y.; Leng, L.; Li, X.; Chen, N.; Zhang, Y. Metal-Organic Framework-Based Molecularly Imprinted Polymer as a High Sensitive and Selective Hybrid for the Determination of Dopamine in Injections and Human Serum Samples. *Biosens. Bioelectron.* **2018**, *118*, 129−136.
(44) Rubio-Govea, R.; Hickey, D. P.; García-Morales, R.; Rodriguez-Delgado, M.; Domínguez-Rovira, M. A.; Minteer, S. D.; Ornelas-Soto, N.; García-García, A. Mos_2 Nanostructured Materials for Electrode Modification in the Development of a Laccase Based Amperometric Biosensor for Non-Invasive Dopamine Detection. *Microchem. J.* **2020**, *155*, No. 104792.
(45) Wang, K.; Liu, P.; Ye, Y.; Li, J.; Zhao, W.; Huang, X. Fabrication of a Novel Laccase Biosensor Based on Silica Nanoparticles Modified with Phytic Acid for Sensitive Detection of Dopamine. *Sens. Actuators, B* **2014**, *197*, 292−299.
(46) Zhou, K.; Shen, D.; Li, X.; Chen, Y.; Hou, L.; Zhang, Y.; Sha, J. Molybdenum Oxide-Based Metal-Organic Framework/Polypyrrole Nanocomposites for Enhancing Electrochemical Detection of Dopamine. *Talanta* **2019**, *209*, No. 120507.
(47) Xie, X.; Wang, D. P.; Guo, C.; Liu, Y.; Rao, Q.; Lou, F.; Li, Q.; Dong, Y.; Li, Q.; Yang, H. B.; Hu, F. X. Single-Atom Ruthenium Biomimetic Enzyme for Simultaneous Electrochemical Detection of Dopamine and Uric Acid. *Anal. Chem.* **2021**, *93*, 4916−4923.
(48) Reddy, S.; Xiao, Q.; Liu, H.; Li, C.; Chen, S.; Wang, C.; Chiu, K.; Chen, N.; Tu, Y.; Ramakrishna, S.; He, L. Bionanotube/Poly(3,4-Ethylenedioxythiophene) Nanohybrid as an Electrode for the Neural Interface and Dopamine Sensor. *ACS Appl. Mater. Interfaces* **2019**, *11*, 18254−18267.
(49) Chen, M.; Cao, X.; Chang, K.; Xiang, H.; Wang, R. A Novel Electrochemical Non-Enzymatic Glucose Sensor Based on Au Nanoparticle-Modified Indium Tin Oxide Electrode and Boronate Affinity. *Electrochim. Acta* **2021**, *368*, No. 137603.
(50) Tseng, T.-F.; Yang, Y.-L.; Chuang, M.-C.; Lou, S.-L.; Galik, M.; Flechsig, G.-U.; Wang, J. Thermally Stable Improved First-Generation Glucose Biosensors Based on Nafion/Glucose-Oxidase Modified Heated Electrodes. *Electrochem. Commun.* **2009**, *11*, 1819−1822.
(51) Mercante, L. A.; Pavinatto, A.; Iwaki, L. E. O.; Scagion, V. P.; Zucolotto, V.; Oliveira, O. N.; Mattoso, L. H. C.; Correa, D. S. Electrospun Polyamide 6/Poly(Allylamine Hydrochloride) Nanofibers Functionalized with Carbon Nanotubes for Electrochemical Detection of Dopamine. *ACS Appl. Mater. Interfaces* **2015**, *7*, 4784−4790.

https://doi.org/10.1021/acsami.1c13446
ACS Appl. Mater. Interfaces 2021, 13, 41753−41772